Abstract

TIAN, MING. A Numerical Simulation of Internal Two-Phase Flow for Aerated-Liquid Injectors. (Under the direction of Dr. Jack R. Edwards.)

Aerated-liquid atomization, which is produced by the introduction of gas directly into a liquid flow immediately upstream of the injector exit orifice to generate a two-phase flow, has been shown to produce well-atomized sprays in a quiescent environment with only a small amount of aerating gas at relatively low injection pressures. A time-derivative preconditioning method using the Low-Diffusion Flux-Splitting Scheme (LDFSS) has been extended to a "mixture" model of two-phase flow and applied to simulate the structure of internal two-phase flow for aerated-liquid injectors, with each phase governed by its own equation of state. The Continuum Surface Force (CSF) model of Brackbill, *et al.* is adapted to model compressible fluid flow influenced by interfacial surface tension. A sub-iterative time integration method based on a planar Gauss-Seidel partitioning of the system matrix is used with implicit source terms as a means of solving the three-dimensional, time-dependent form of the governing equations. The calculations are parallelized using domain-decomposition and Message-Passing Interface (MPI) methods, and are optimized for operation on the 720 processor IBM SP-2 at the North Carolina Supercomputing Center (NCSC). Simulation results for 2-D aerated-liquid injector flowfields at gas-to-liquid (GLR) mass ratios of 0.08% and 2.45% are discussed. In accord with experimental visualization data, the results for $GLR = 0.08\%$ indicate a combination of slugging and core-annular two-phase flow in the injector. Results at $GLR = 2.45\%$ indicate that a core-annular flow mode dominates, again in agreement with experimental results. The effects of the choice of reference velocity and the level of surface tension on the injector flowfield solutions are also examined.

A Numerical Simulation of Internal Two-Phase Flow for Aerated-Liquid Injectors

by

Ming Tian

A thesis submitted to the Graduate Faculty of
North Carolina State University
in partial fulfillment of the
requirements for the Degree of
Master of Science

Department of Mechanical and Aerospace Engineering

Raleigh, North Carolina
September 11, 2002

Approved By:

Dr. S. V. Tsynkov, Member

Dr. H. A. Hassan, Member

Dr. J. R. Edwards, Chair

Biography

Ming Tian was born in Chengdu, Sichuan, China on April 6, 1974 to Tianrong Ni and Zuyang Tian. Raised in Chengdu, Sichuan, he graduated from Number 12 High School of Chengdu in 1992. He later received Bachelor of Engineering degrees in Aerodynamics from Beijing University of Aeronautics and Astronautics in 1996. Ming came to the United States on August, 2000, and is currently attaining a Master of Science degree in Aerospace Engineering at North Carolina State University. He will continue to pursue a Doctor of Philosophy degree at the same University from Fall, 2002.

Acknowledgments

First, I would like to thank my parents for guiding me through my first steps of life and education. I would also like to thank my advisor, Dr. Jack R. Edwards, who has guided my academic and professional development for the past two years. I would also like to thank my loving wife, Yu Chen, who has been supportive of me and my study throughout my graduate educations. Thanks also due to every instructor who taught me in the past two years, and every colleague in Hypersonics Lab, 4216 Broughton Hall, for all the help and support in my study in the United States.

I would like to acknowledge Taitech, Inc. for sponsoring this research under subcontract from the Air Force Research Laboratory, Wright-Patterson AFB. I also acknowledge the North Carolina Supercomputing Center for granting IBM SP-2 computer time and continuously supporting my research computations.

Table of Contents

List of Tables

List of Figures

List of Symbols

Roman symbols:

A	area
a	sound speed
C_p	specific heat at constant pressure
$\mathbf{E}, \mathbf{F}, \mathbf{G}$	inviscid flux vector in ξ, η, ζ directions
$\mathbf{E_v}, \mathbf{F_v}, \mathbf{G_v}$	viscous flux vector in ξ, η, ζ directions
g	gravity acceleration
H	total enthalpy per mass of mixture
h	mixture enthalpy per mass
h	phase interface thickness in continuum surface force model
i, j, k	indices corresponding to ξ, η, and ζ directions
J	Jacobian of coordinate transformation
M	Mach number
m	mass
N_g	number of gas components
N_l	number of liquid components
$\hat{n}$	unit vector normal to a surface
$\mathbf{P}$	preconditioning matrix
p	pressure
Pr	Prandtl number
q_i	heat flux vector
R	the discrete representation of the steady part of governing equation set
$\mathbf{R}$	Residual vector
$\mathcal{R}$	universal gas constant
$\mathcal{R}_{mix}$	specific gas constant of the mixture gas
Re	Reynolds number
$\mathbf{S}$	source term vector
Sc	Schmidt number
t	time
T	temperature
$\mathbf{U}$	vector of conservative variables
u, v, w	Cartesian velocities in x, y, z directions
u_i^d, v_i^d, w_i^d	Cartesian molecular diffusion velocities of component i in gas phase
u_i	Cartesian velocity in index notation
$\mathcal{U}, \mathcal{V}, \mathcal{W}$	contravariant velocities in ξ, η, ζ directions
$\mathcal{U}_i^d, \mathcal{V}_i^d, \mathcal{W}_i^d$	contravariant diffusion velocities of species i in gas phase in ξ, η, ζ directions
$\mathbf{V}$	vector of primitive variables
V	total volume of the system or grid cell volume
V_g, V_l	actual volume of gas phase and actual volume of liquid phase
$W_{g,i}$	molecular weight of component i in gas phase

x, y, z	Cartesian coordinates
x_i	Cartesian coordinate in index notation
$\mathbf{x}$	location vector
Y_g	mass fraction of gas phase in the mixture
$Y_{g,i}$	mass fraction of component i in gas phase
Y_l	mass fraction of liquid phase in the mixture
$Y_{l,j}$	mass fraction of component j in liquid phase

Greek symbols:

α	volume fraction
δ	delta function in derivation of surface tension
δ_{ij}	Kronecker delta
κ	curvature in surface tension
λ	thermal conductivity coefficient or eigenvalue
μ	laminar viscosity
ξ, η, ζ	generalized coordinates
ξ_i	generalized coordinate in index notation
ρ	mixture density
σ	fluid surface tension coefficient
τ_{ij}	stress tensor
$\chi_{g,i}$	mole fraction of component i in gas phase

Subscripts:

$\frac{1}{2}$	represents a numerical interface quantity
∞	represents a freestream quantity
g	represents a property in gas phase
i, j, k	represents spatial coordinates or cell indices
l	represents a property in liquid phase
m	represents chemical species
p	represents partial derivative with respect to variable p
T	represents partial derivative with respect to variable T

Superscripts:

c	represents convective component in flux vector
k	represents pseudo time level
n	represents physical time level
p	represents pressure component in flux vector
T	represents the transpose of a matrix

0 Introduction

The successful design of a liquid-fueled, air-breathing propulsion system depends to a significant extent on liquid atomization performance, which determines the mixing behavior and the combustion efficiency of the combustor. Aerated-liquid atomization, which is produced by the introduction of gas directly into a liquid flow immediately upstream of the injector exit orifice to generate a two-phase flow, has been shown to produce well-atomized sprays in a quiescent environment with only a small amount of aerating gas at relatively low injection pressures.

Two different modes of spray structures for aerated-liquid jets in high-speed crossflows were identified by Lin, *et al.* [1]: pure liquid-mode spray and aerating-mode spray. As the amount of aerating gas in the liquid jet increases, the aerated-liquid jet transits from the dual-mode spray to pure aerating-mode spray as a steady co-annular column structure is reached.

The structures of the internal two-phase flow inside the aerated-liquid injector and the structures of corresponding sprays under various aeration levels have been explored experimentally by Lin, *et al.* [1] The U.S. Air Force is interested in applying aerated-liquid atomization as a means of producing smaller droplets that may vaporize faster. However, the numerical simulations of the structures of the internal two-phase flow inside the aerated-liquid injector and the structures of corresponding sprays have not been systematically studied.

The present study intends to numerically investigate the two-phase flow inside aerated-liquid atomizers in order to understand the mechanisms that may lead to the formation of smaller droplets. As an initial step, a three-dimensional Navier-Stokes solver for a "mixture" model of two-phase flow is developed. This code is based on the combination of time-derivative preconditioning [2, 3, 4, 5, 6, 7, 8] and low-diffusion upwinding methods [9, 10] and is designed to capture the time-dependent

motion of two-phase flow features, such as gas bubble growth in a liquid injector. In this study, aspects of the numerical and physical modeling of this two-phase flow are systematically investigated to understand their effects on the injector flowfield solution.

Section 1 gives the derivation of two-phase mixture model utilized in the current study. Section 2 introduces the preconditioning method and presents an extension of the Low-Diffusion Flux-Splitting Scheme valid for two-phase mixture flows. Section 3 formulates the geometry, and presents initial and boundary conditions. Section 4 presents and discusses the results of several simulations of a two-dimensional aerated-liquid injector flowfield at two gas-to-liquid (GLR) mass ratios. Sections 5 and 6 give the conclusions and future work, respectively. Finally, derivations of the real fluid sound speed, eigenvalues of the preconditioned system and interface flux Jacobian matrices are presented in Appendix A, B and C, respectively.

1 Derivation of Two-Phase Mixture Model

Requisite to any numerical investigation is a thorough understanding of the principles and equations that represent those principles. In this section, the two-phase mixture model used in this study is developed. In order to get a better understanding of the two-phase flow mixture model, we start with some definitions used in the model. In general, subscripts "g" and "l" refer to "gas phase" and "liquid phase" respectively.

1.1 Definitions

A number of flow terms are briefly introduced in this section and further elaborated on in subsequent sections, such as volume fraction, bulk density, mass fraction, mole fraction and mass-averaged velocity.

- Volume Fraction

  Volume fraction represents the volume occupied by a particular phase, referenced to the system volume. In the two-phase model, there are two phases, gas phase and liquid phase . For the gas phase, the gas volume fraction is defined as:

$$\alpha_g = \frac{V_g}{V} \tag{1.1}$$

  where V_g is the volume of the gas phase, and V is the total volume of the system, which can be written as $V = V_g + V_l$, where V_l is the volume of the liquid phase. Similarly, the liquid volume fraction is defined as:

$$\alpha_l = \frac{V_l}{V} = \frac{V - V_g}{V} = 1 - \alpha_g \tag{1.2}$$

  In general, for a system with n phases, the volume fraction of phase k is the ratio of the volume of phase k to the total volume of the system and is written

as:

$$\alpha_k = \frac{V_k}{\sum_{m=1}^{n} V_m} \tag{1.3}$$

with the following constraint:

$$\sum_{k=1}^{n} \alpha_k = 1 \tag{1.4}$$

- Bulk Density

  The bulk density of the mixture of the two-phase system is defined as:

$$\rho = \rho_g \alpha_g + \rho_l \alpha_l \tag{1.5}$$

$$\rho_g = \sum_{k=1}^{N_g} \rho_{g,k} \tag{1.6}$$

$$\rho_l = \sum_{k=1}^{N_l} \rho_{l,k} \tag{1.7}$$

  where ρ_g and ρ_l are the actual densities of the gas phase and liquid phase respectively, $\rho_{g,i}$ is the density of component i in the gas phase, and $\rho_{l,j}$ is the density of component j in the liquid phase.

  In general, for a system with n phases, the following constraint holds:

$$\rho = \sum_{k=1}^{n} \rho_k \alpha_k \tag{1.8}$$

  where ρ_k is the actual density of phase k.

- Mass Fraction

  In the two-phase system, the mass fraction of gas phase, Y_g, is a ratio of the mass of gas phase to the total mass of the system, and written as:

$$Y_g = \frac{m_g}{m} = \frac{\rho_g V_g}{\rho V} = \frac{\rho_g V_g / V}{\rho} = \frac{\rho_g \alpha_g}{\rho_g \alpha_g + \rho_l \alpha_l} \tag{1.9}$$

where m_g is the mass of the gas phase, and m is the total mass of the system. Similarly, the mass fraction of the liquid phase is defined as:

$$Y_l = \frac{\rho_l \alpha_l}{\rho_g \alpha_g + \rho_l \alpha_l} = 1 - Y_g \tag{1.10}$$

Furthermore, if the gas phase consists of N_g components, then the mass fraction of component i in the gas phase is defined as:

$$Y_{g,i} = \frac{m_{g,i}}{m_g} = \frac{\rho_{g,i} V_g}{\rho_g V_g} = \frac{\rho_{g,i}}{\sum_{k=1}^{N_g} \rho_{g,k}} \tag{1.11}$$

$$\text{and} \qquad \sum_{k=1}^{N_g} Y_{g,k} = 1 \tag{1.12}$$

where $m_{g,i}$ is the mass of component i in the gas phase, and m_g is the mass of the gas phase.

Similarly, if the liquid phase consists of N_l components, then the mass fraction of component j in the liquid phase is defined as:

$$Y_{l,j} = \frac{m_{l,j}}{m_l} = \frac{\rho_{l,j} V_l}{\rho_l V_l} = \frac{\rho_{l,j}}{\sum_{k=1}^{N_l} \rho_{l,k}} \tag{1.13}$$

$$\text{and} \qquad \sum_{k=1}^{N_l} Y_{l,k} = 1 \tag{1.14}$$

where $m_{l,j}$ is the mass of component j in the liquid phase, and m_l is the mass of the liquid phase.

In general, for a system with n phases, the mass fraction of phase k is the ratio of the mass of phase k to the total mass of the system, and is written as:

$$Y_k = \frac{\rho_k \alpha_k}{\sum_{m=1}^{n} \rho_m \alpha_m} \tag{1.15}$$

with the following constraint:

$$\sum_{k=1}^{n} Y_k = 1 \tag{1.16}$$

- Mole Fraction

  In the derivation of gas mixture transport models, the concept of mole fraction may be used. The mole fraction of gas species k is defined as:

$$\chi_{g,k} = \frac{\frac{\rho_{g,k}}{W_{g,k}}}{\sum_{m=1}^{N_g} \frac{\rho_{g,m}}{W_{g,m}}} \tag{1.17}$$

  where $W_{g,k}$ is the molecular weight of gas species k.

- Mass-Averaged Velocity

  In the two-phase mixture system, the mass-averaged velocity is defined as:

$$u_i = \left(\rho_g \alpha_g u_{ig} + \rho_l \alpha_l u_{il}\right)/\rho = Y_g u_{ig} + Y_l u_{il}, \tag{1.18}$$

  where u_{ig} is the velocity of gas phase and u_{il} is the velocity of liquid phase in index notation. Thus, u_{ig} and u_{il} can be expressed as

$$\begin{array}{rclcl} u_{ig} & = & u_i + u_{ig} - u_i & = & u_i + Y_l u_{ir}, \\ u_{il} & = & u_i + u_{il} - u_i & = & u_i - Y_g u_{ir}, \end{array} \tag{1.19}$$

  where u_{ir} is the relative velocity, $u_{ir} = u_{ig} - u_{il}$. If $u_{ir} = 0$, then we have $u_{ig} = u_{il} = u_i$. This is called kinematic equilibrium.

1.2 Governing Equations

In this section, the governing equations for two-phase flow are firstly derived in Cartesian coordinates, then they are transformed into generalized coordinates.

1.2.1 Derivation of the Mixture Equations

The two-phase flow problems considered herein are assumed to be governed by the Navier-Stokes equations, expanded to include separate transport equations for each relevant chemical species. This set of equations is simply a recasting of the following conservation laws:

Conservation of Mass

Conservation of Momentum

Conservation of Energy

The equation of the application of the Conservation of Mass law to a fluid flow is called a continuity equation. Similarly, when the law of Conservation of Momentum (i.e. Newton's Second Law) is applied to a fluid flow, the resulting equations are referred to as momentum equations. Finally, application of the Conservation of Energy law to a fluid flow yields an energy equation.

In the two-phase mixture system, we suppose there are N_g components in the gas phase and N_l components in the liquid phase. Each component has its own continuity, momentum and energy equations. However, we don't solve all of them. In our two-phase mixture model, we solve $N_g - 1$ continuity equations for the gas phase, $N_l - 1$ continuity equations for the liquid phase, one phasic continuity equation, one mixture continuity equation, three mixture momentum equations, and one mixture energy equations.

In the derivation of the two-phase mixture model, mass-averaged velocities are utilized. For instance, we sum up two phasic continuity equations, which can be expressed as:

$$\begin{aligned} \frac{\partial(\rho Y_g)}{\partial t} &+ \frac{\partial(\rho Y_g u_{ig})}{\partial x_i} &= 0, \\ \frac{\partial(\rho Y_l)}{\partial t} &+ \frac{\partial(\rho Y_l u_{il})}{\partial x_i} &= 0, \end{aligned} \tag{1.20}$$

to get the mixture continuity equation,

$$\frac{\partial(\rho Y_g + \rho Y_l)}{\partial t} + \frac{\partial(\rho Y_g u_{ig} + \rho Y_l u_{il})}{\partial x_i} = 0. \tag{1.21}$$

Introducing the mass-averaged velocity leads to:

$$\frac{\partial \rho}{\partial t} + \frac{\partial(\rho u_i)}{\partial x_i} = 0. \tag{1.22}$$

Similarly, the mixture momentum equations can be derived as:

$$\frac{\partial(\rho u_i)}{\partial t} + \frac{\partial}{\partial x_i}(\rho u_i u_j + \rho Y_g Y_l u_{ir} u_{jr} + \delta_{ij} p - \tau_{ij}) = 0. \tag{1.23}$$

The kinematic equilibrium drift-flow model is used to relate the relative velocities to other variables. This simple closure assumes that $u_{ig} = u_{il}$, or $u_{ir} = 0$. It means that the momentum transfer between phases is fast enough so that velocities are the same. Thus, the mixture momentum equations can be simplified as:

$$\frac{\partial(\rho u_i)}{\partial t} + \frac{\partial}{\partial x_i}(\rho u_i u_j + \delta_{ij} p - \tau_{ij}) = 0. \tag{1.24}$$

Furthermore, we assume that phases are in thermal equilibrium. That means that the two phases have the common temperature. Having these assumptions, we get only one energy equation for the mixture system. It can be expressed as:

$$\frac{\partial(\rho H - p)}{\partial t} + \frac{\partial}{\partial x_i}(\rho H u_i - u_j \tau_{ij} + q_i) = 0. \tag{1.25}$$

The stress tensor, the heat flux, and the total enthalpy per unit mass are given by

$$\tau_{ij} = \mu\left(\frac{\partial u_i}{\partial x_j} + \frac{\partial u_j}{\partial x_i}\right) - \frac{2}{3}\delta_{ij}\mu\frac{\partial u_k}{\partial x_k} \tag{1.26}$$

$$q_i = -\lambda\frac{\partial T}{\partial x_i} \tag{1.27}$$

$$H = h + \frac{1}{2}{u_i}^2 \tag{1.28}$$

where μ is the mixture viscosity, λ is the mixture thermal conductivity, and h is the mixture enthalpy per unit mass. These mixture thermodynamic and transport properties will be detailed in Section 1.3.

1.2.2 Vector form of the Conservation Equations

Including gravity and surface tension, the governing equations can be written in strong conservation law, vector form for Cartesian coordinates as:

$$\frac{\partial \mathbf{U}}{\partial t} + \frac{\partial (\mathbf{E} - \mathbf{E_v})}{\partial x} + \frac{\partial (\mathbf{F} - \mathbf{F_v})}{\partial y} + \frac{\partial (\mathbf{G} - \mathbf{G_v})}{\partial z} = \mathbf{S} \tag{1.29}$$

where $\mathbf{U}$ is the vector of conservative variables, $\mathbf{E}$, $\mathbf{F}$ and $\mathbf{G}$ are the inviscid fluxes, $\mathbf{E_v}$, $\mathbf{F_v}$ and $\mathbf{G_v}$ are the viscous fluxes, and $\mathbf{S}$ is the vector of source terms, expressed separately as

$$\mathbf{U} = \begin{bmatrix} \rho Y_{g,1} Y_g \\ \vdots \\ \rho Y_{g,N_g-1} Y_g \\ \rho Y_g \\ \rho \\ \rho u \\ \rho v \\ \rho w \\ \rho H - p \\ \rho Y_{l,1} Y_l \\ \vdots \\ \rho Y_{l,N_l-1} Y_l \end{bmatrix}, \tag{1.30}$$

$$\mathbf{E} = \begin{bmatrix} \rho Y_{g,1} Y_g u \\ \vdots \\ \rho Y_{g,N_g-1} Y_g u \\ \rho Y_g u \\ \rho u \\ \rho u^2 + p \\ \rho v u \\ \rho w u \\ \rho H u \\ \rho Y_{l,1} Y_l u \\ \vdots \\ \rho Y_{l,N_l-1} Y_l u \end{bmatrix}, \mathbf{F} = \begin{bmatrix} \rho Y_{g,1} Y_g v \\ \vdots \\ \rho Y_{g,N_g-1} Y_g v \\ \rho Y_g v \\ \rho v \\ \rho u v \\ \rho v^2 + p \\ \rho w v \\ \rho H v \\ \rho Y_{l,1} Y_l v \\ \vdots \\ \rho Y_{l,N_l-1} Y_l v \end{bmatrix}, \mathbf{G} = \begin{bmatrix} \rho Y_{g,1} Y_g w \\ \vdots \\ \rho Y_{g,N_g-1} Y_g w \\ \rho Y_g w \\ \rho w \\ \rho u w \\ \rho v w \\ \rho w^2 + p \\ \rho H w \\ \rho Y_{l,1} Y_l w \\ \vdots \\ \rho Y_{l,N_l-1} Y_l w \end{bmatrix}, \tag{1.31}$$

$$\mathbf{E_v} = \begin{bmatrix} -\rho Y_{g,1} Y_g u_1^d \\ \vdots \\ -\rho Y_{g,N_g-1} Y_g u_{N_g-1}^d \\ 0 \\ 0 \\ \tau_{xx} \\ \tau_{yx} \\ \tau_{zx} \\ u_i \tau_{ix} - q_x \\ 0 \\ \vdots \\ 0 \end{bmatrix}, \mathbf{F_v} = \begin{bmatrix} -\rho Y_{g,1} Y_g v_1^d \\ \vdots \\ -\rho Y_{g,N_g-1} Y_g v_{N_g-1}^d \\ 0 \\ 0 \\ \tau_{xy} \\ \tau_{yy} \\ \tau_{zy} \\ u_i \tau_{iy} - q_y \\ 0 \\ \vdots \\ 0 \end{bmatrix}, \tag{1.32}$$

$$\mathbf{G_v} = \begin{bmatrix} -\rho Y_{g,1} Y_g w_1^d \\ \vdots \\ -\rho Y_{g,N_g-1} Y_g w_{N_g-1}^d \\ 0 \\ 0 \\ \tau_{xz} \\ \tau_{yz} \\ \tau_{zz} \\ u_i \tau_{iz} - q_z \\ 0 \\ \vdots \\ 0 \end{bmatrix}, \mathbf{S} = \begin{bmatrix} 0 \\ \vdots \\ 0 \\ 0 \\ 0 \\ \mathrm{F}_{sv,x} + \rho g \\ \mathrm{F}_{sv,y} \\ \mathrm{F}_{sv,z} \\ \mathrm{F}_{sv,x_i} u_i + \rho g u \\ 0 \\ \vdots \\ 0 \end{bmatrix}, \tag{1.33}$$

$$\mathbf{F_{sv}} = \mathrm{F}_{sv,x}\,\vec{\mathrm{i}} + \mathrm{F}_{sv,y}\,\vec{\mathrm{j}} + \mathrm{F}_{sv,z}\,\vec{\mathrm{k}}, \tag{1.34}$$

where u_i^d, v_i^d, w_i^d are diffusion velocities for component i in gas phase, which will be described in Section 1.3.2. $\mathbf{F_{sv}}$ is the surface tension force between gas phase and liquid phase, which will be described in Section 1.4. The gravity force is assumed to be aligned with the x direction. In Equations 1.32 and 1.33, index notation is used to simplify the formulations.

In this two-phase mixture model, the mixture density, ρ, and the mixture en-

thalpy, h, are functions of mass fractions, pressure and temperature,

$$\begin{aligned} \rho &= \rho\left(Y_g, Y_{g,i}, Y_{l,j}, p, T\right), && (1.35) \\ h &= h\left(Y_g, Y_{g,i}, Y_{l,j}, p, T\right), && (1.36) \\ \text{where} \quad i &= 1, \cdots, N_g, \quad j = 1, \cdots, N_l \end{aligned}$$

General procedures for deriving equations of two-phase flows may be found in Reference 11.

1.2.3 Coordinate Transformation

The governing equations may be written for a generalized coordinate system (ξ, η, ζ) according to the transformation

$$\begin{aligned} \xi &= \xi(x, y, z) \\ \eta &= \eta(x, y, z) \\ \zeta &= \zeta(x, y, z). \end{aligned} \tag{1.37}$$

with respect to the Cartesian coordinate system (x, y, z). This has the advantage of using a uniform computational grid to represent the problem while it may be physically represented in any other coordinate system. Using the chain rule of differentiation, the partial derivatives may be expressed as

$$\begin{aligned} \frac{\partial}{\partial x} &= \xi_x \frac{\partial}{\partial \xi} + \eta_x \frac{\partial}{\partial \eta} + \zeta_x \frac{\partial}{\partial \zeta} \\ \frac{\partial}{\partial y} &= \xi_y \frac{\partial}{\partial \xi} + \eta_y \frac{\partial}{\partial \eta} + \zeta_y \frac{\partial}{\partial \zeta} \\ \frac{\partial}{\partial z} &= \xi_z \frac{\partial}{\partial \xi} + \eta_z \frac{\partial}{\partial \eta} + \zeta_z \frac{\partial}{\partial \zeta}. \end{aligned} \tag{1.38}$$

The governing equations, written in strong conservation law, vector form for generalized coordinates, are

$$\frac{1}{J}\frac{\partial \mathbf{U}}{\partial t} + \frac{\partial(\mathbf{E} - \mathbf{E_v})}{\partial \xi} + \frac{\partial(\mathbf{F} - \mathbf{F_v})}{\partial \eta} + \frac{\partial(\mathbf{G} - \mathbf{G_v})}{\partial \zeta} = \mathbf{S} \tag{1.39}$$

The governing equation set is expanded here to include continuity equations for both gas phase components and liquid phase components, where $\mathbf{U}$ is the vector of conservative variables, $\mathbf{E}$, $\mathbf{F}$ and $\mathbf{G}$ are the inviscid fluxes, $\mathbf{E_v}$, $\mathbf{F_v}$ and $\mathbf{G_v}$ are the viscous fluxes, and $\mathbf{S}$ is the vector of source terms, expressed separately as

$$\mathbf{U} = \begin{bmatrix} \rho Y_{g,1} Y_g \\ \vdots \\ \rho Y_{g,N_g-1} Y_g \\ \rho Y_g \\ \rho \\ \rho u \\ \rho v \\ \rho w \\ \rho H - p \\ \rho Y_{l,1} Y_l \\ \vdots \\ \rho Y_{l,N_l-1} Y_l \end{bmatrix}, \tag{1.40}$$

$$\mathbf{E} = \frac{1}{J} \begin{bmatrix} \rho Y_{g,1} Y_g \mathcal{U} \\ \vdots \\ \rho Y_{g,N_g-1} Y_g \mathcal{U} \\ \rho Y_g \mathcal{U} \\ \rho \mathcal{U} \\ \rho u \mathcal{U} + \xi_x p \\ \rho v \mathcal{U} + \xi_y p \\ \rho w \mathcal{U} + \xi_z p \\ \rho H \mathcal{U} \\ \rho Y_{l,1} Y_l \mathcal{U} \\ \vdots \\ \rho Y_{l,N_l-1} Y_l \mathcal{U} \end{bmatrix}, \mathbf{F} = \frac{1}{J} \begin{bmatrix} \rho Y_{g,1} Y_g \mathcal{V} \\ \vdots \\ \rho Y_{g,N_g-1} Y_g \mathcal{V} \\ \rho Y_g \mathcal{V} \\ \rho \mathcal{V} \\ \rho u \mathcal{V} + \eta_x p \\ \rho v \mathcal{V} + \eta_y p \\ \rho w \mathcal{V} + \eta_z p \\ \rho H \mathcal{V} \\ \rho Y_{l,1} Y_l \mathcal{V} \\ \vdots \\ \rho Y_{l,N_l-1} Y_l \mathcal{V} \end{bmatrix}, \mathbf{G} = \frac{1}{J} \begin{bmatrix} \rho Y_{g,1} Y_g \mathcal{W} \\ \vdots \\ \rho Y_{g,N_g-1} Y_g \mathcal{W} \\ \rho Y_V \mathcal{W} \\ \rho \mathcal{W} \\ \rho u \mathcal{W} + \zeta_x p \\ \rho v \mathcal{W} + \zeta_y p \\ \rho w \mathcal{W} + \zeta_z p \\ \rho H \mathcal{W} \\ \rho Y_{l,1} Y_l \mathcal{W} \\ \vdots \\ \rho Y_{l,N_l-1} Y_l \mathcal{W} \end{bmatrix}, \tag{1.41}$$

$$\mathbf{E_v} = \frac{1}{J}\begin{bmatrix} -\rho Y_{g,1} Y_g \mathcal{U}_1^d \\ \vdots \\ -\rho Y_{g,N_g-1} Y_g \mathcal{U}_{N_g-1}^d \\ 0 \\ 0 \\ \xi_{x_i}\tau_{i1} \\ \xi_{x_i}\tau_{i2} \\ \xi_{x_i}\tau_{i3} \\ \xi_{x_i}(u_j\tau_{ij} - q_i) \\ 0 \\ \vdots \\ 0 \end{bmatrix}, \mathbf{F_v} = \frac{1}{J}\begin{bmatrix} -\rho Y_{g,1} Y_g \mathcal{V}_1^d \\ \vdots \\ -\rho Y_{g,N_g-1} Y_g \mathcal{V}_{N_g-1}^d \\ 0 \\ 0 \\ \eta_{x_i}\tau_{i1} \\ \eta_{x_i}\tau_{i2} \\ \eta_{x_i}\tau_{i3} \\ \eta_{x_i}(u_j\tau_{ij} - q_i) \\ 0 \\ \vdots \\ 0 \end{bmatrix}, \tag{1.42}$$

$$\mathbf{G_v} = \frac{1}{J}\begin{bmatrix} -\rho Y_{g,1} Y_g \mathcal{W}_1^d \\ \vdots \\ -\rho Y_{g,N_g-1} Y_g \mathcal{W}_{N_g-1}^d \\ 0 \\ 0 \\ \zeta_{x_i}\tau_{i1} \\ \zeta_{x_i}\tau_{i2} \\ \zeta_{x_i}\tau_{i3} \\ \zeta_{x_i}(u_j\tau_{ij} - q_i) \\ 0 \\ \vdots \\ 0 \end{bmatrix}, \mathbf{S} = \frac{1}{J}\begin{bmatrix} 0 \\ \vdots \\ 0 \\ 0 \\ 0 \\ \mathrm{F}_{sv,\xi} + \rho g \\ \mathrm{F}_{sv,\eta} \\ \mathrm{F}_{sv,\zeta} \\ \mathrm{F}_{sv,\xi_i} u_i + \rho g u \\ 0 \\ \vdots \\ 0 \end{bmatrix}, \tag{1.43}$$

$$\mathbf{F_{sv}} = \mathrm{F}_{sv,\xi}\,\vec{\xi} + \mathrm{F}_{sv,\eta}\,\vec{\eta} + \mathrm{F}_{sv,\zeta}\,\vec{\zeta} \tag{1.44}$$

In the above development, $\mathcal{U}$, $\mathcal{V}$, and $\mathcal{W}$ are the contravariant velocity components,

$$\begin{aligned} \mathcal{U} &\equiv \xi_x u + \xi_y v + \xi_z w \\ \mathcal{V} &\equiv \eta_x u + \eta_y v + \eta_z w \\ \mathcal{W} &\equiv \zeta_x u + \zeta_y v + \zeta_z w, \end{aligned} \tag{1.45}$$

$\mathcal{U}_i^d$, $\mathcal{V}_i^d$, and $\mathcal{W}_i^d$ are the contravariant diffusion velocities for component i in gas phase,

$$\begin{aligned} \mathcal{U}_i^d &\equiv \xi_x u_i^d + \xi_y v_i^d + \xi_z w_i^d \\ \mathcal{V}_i^d &\equiv \eta_x u_i^d + \eta_y v_i^d + \eta_z w_i^d \\ \mathcal{W}_i^d &\equiv \zeta_x u_i^d + \zeta_y v_i^d + \zeta_z w_i^d, \end{aligned} \tag{1.46}$$

and the Jacobian of the coordinate transformation J is defined and evaluated as [12]

$$J = 1/J^{-1} = \frac{1}{\dfrac{\partial(x,y,z)}{\partial(\xi,\eta,\zeta)}} = \frac{1}{\begin{vmatrix} x_\xi & x_\eta & x_\zeta \\ y_\xi & y_\eta & y_\zeta \\ z_\xi & z_\eta & z_\zeta \end{vmatrix}} \tag{1.47}$$

where x_ξ, x_η, x_ζ, y_ξ, y_η, y_ζ, z_ξ, z_η, and z_ζ are the inverse metric derivatives and are evaluated by second-order finite differences. Notice that $1/J$ is a measure of the cell volume.

1.3 Thermodynamic and Transport Models

This section is a summary of the relationships between the mean flow variables, with discussions regarding the calculation of various fluid properties. The equations presented in this section are used to close the problem equation set.

1.3.1 Thermodynamic Models for Gas Phase

For the gas phase, the ideal gas state equation is used to get a relation between pressure, temperature and gas density. Thus, the equation of state for the gas phase is given as

$$\rho_g = \rho_g(p,T) = \frac{p}{\mathcal{R}_{mix}T}, \tag{1.48}$$

where $\mathcal{R}_{mix}$, the mixture value for the specific gas constant, is a weighted average of the individual specific gas constants of the constituent components at constant pressure. It is written as

$$\mathcal{R}_{mix} = \sum_{k=1}^{N_g} \frac{Y_{g,k}}{W_{g,k}}\mathcal{R}, \tag{1.49}$$

where $\mathcal{R}$ is the universal gas constant and $W_{g,k}$ is the molecular weight of gas species k.

The specific heat at constant pressure and enthalpy of gas mixture are defined

as:

$$C_{p,g} = \sum_{k=1}^{N_g} Y_{g,k} C_{p,k}, \tag{1.50}$$

$$h_g = \sum_{k=1}^{N_g} Y_{g,k} h_{g,k}, \tag{1.51}$$

where $C_{p,k}$ is the specific heat of gas species k, and $h_{g,k}$ is the enthalpy of gas species k. These properties are given by polynomial curve-fits:

$$C_{p,k} = \frac{\mathcal{R}}{W_{g,k}} \left(a_{1,k} + a_{2,k} T + a_{3,k} T^2 + a_{4,k} T^3 + a_{5,k} T^4 \right), \tag{1.52}$$

$$h_{g,k} = \frac{\mathcal{R}}{W_{g,k}} T \left(a_{1,k} + \frac{1}{2} a_{2,k} T + \frac{1}{3} a_{3,k} T^2 + \frac{1}{4} a_{4,k} T^3 + \frac{1}{5} a_{5,k} T^4 + \frac{b_{1,k}}{T} \right), \tag{1.53}$$

where $a_{i,k}$ $(i = 1, 2, 3, 4, 5)$ and $b_{1,k}$ are curve-fit coefficients for gas species k and obtained from McBride, *et al.* [13]

1.3.2 Molecular Transport Models for Gas Phase

The molecular viscosity, $\mu_{g,i}$, of each component of the gas mixture is modeled using Sutherland's formula as:

$$\mu_{g,i} = \mu_{0,i} \left(\frac{T}{T_{0,i}} \right)^{\frac{3}{2}} \frac{T_{0,i} + S_i}{T + S_i} \tag{1.54}$$

where $\mu_{0,i}$, $T_{0,i}$ and S_i are constants of gas species i. In the current work, there are two gas components, water vapor and nitrogen, and one liquid component, water. Thus, these constants are listed in Table 1.1.

Table 1.1: Constants for molecular transport of gas

Species i	Name	$\mu_{0,i}$	$T_{0,i}$	S_i
1	H_2O	1.703×10^{-5}	273.1	138.6
2	N_2	1.663×10^{-5}	273.1	106.7

Wilke's formula [14] is then applied to model the gas mixture molecular viscosity as:

$$\mu_g = \sum_{i=1}^{N_g} \frac{\chi_{g,i}\mu_{g,i}}{\sum_{j=1}^{N_g} \chi_{g,j}\phi_{ij}} \tag{1.55}$$

where

$$\phi_{ij} = \frac{\left[1 + \left(\frac{\mu_{g,i}}{\mu_{g,j}}\right)^{\frac{1}{2}} \left(\frac{W_{g,j}}{W_{g,i}}\right)^{\frac{1}{4}}\right]^2}{\sqrt{8}\left(1 + \frac{W_{g,i}}{W_{g,j}}\right)^{\frac{1}{2}}} \tag{1.56}$$

and $\chi_{g,i}$ is the mole fraction of gas species i.

The molecular thermal conductivity of gas mixture, λ_g, is modeled using the Prandtl number such that

$$\lambda_g = \frac{C_{p,g}\mu_g}{Pr}, \tag{1.57}$$

where the Prandtl number, Pr, is chosen to be 0.72 in the current work.

The molecular diffusion velocities of the i^{th} component in gas phase in the j^{th} direction, $u^d_{i,j}$, are expressed using Fick's law as:

$$u^d_{i,j} = -\frac{\mathcal{D}_i}{Y_{g,i}} \frac{\partial Y_{g,i}}{\partial x_j}, \tag{1.58}$$

where $\mathcal{D}_i$ represents the diffusion coefficient for component i in gas phase. Fick's law can be rewritten using the mixture density ρ, the gas mixture viscosity μ_g, and the gas phase volume fraction by way of the Schmidt number, $Sc = \frac{\mu_g \alpha_g}{\rho Y_g \mathcal{D}}$,

$$\rho Y_{g,i} Y_g u^d_{i,j} = -\frac{\mu_g \alpha_g}{Sc} \frac{\partial Y_{g,i}}{\partial x_j}. \tag{1.59}$$

A constant Schmidt number is assumed, having value of 0.5, which implies the specification of only one diffusion coefficient for all gas phase components.

1.3.3 Thermodynamic and Transport Models for Liquid Phase

The generalized Tait equation of state is incorporated to relate the pressure, temperature, and liquid density variables for the liquid phase components. The state

equation is written as [15]:

$$\frac{\rho_l}{\rho_{l,sat}} = \left(1 + \frac{p - p_{sat}}{3.0 \times 10^8}\right)^{1/7}, \tag{1.60}$$

where p_{sat} is the saturation pressure, and $\rho_{l,sat}$ is the saturation density for liquid. These saturation properties are given in convenient forms in Reference 16:

$$\ln \frac{p_{sat}}{p_c} = \frac{T_c}{T}\left(a_1\theta + a_2\theta^{1.5} + a_3\theta^3 + a_4\theta^{3.5} + a_5\theta^4 + a_6\theta^{7.5}\right), \tag{1.61}$$

$$\frac{\rho_{l,sat}}{\rho_c} = 1 + b_1\theta^{\frac{1}{3}} + b_2\theta^{\frac{2}{3}} + b_3\theta^{\frac{5}{3}} + b_4\theta^{\frac{16}{3}} + b_5\theta^{\frac{43}{3}} + b_6\theta^{\frac{110}{3}}, \tag{1.62}$$

where $\theta = 1 - \frac{T}{T_c}$, and p_c, T_c and ρ_c represent the critical pressure, temperature, and density, respectively. The critical conditions for water are $p_c = 22.64 \times 10^5$ Pa, $T_c = 647.14$ K, and $\rho_c = 332$ kg/m^3. The coefficients a_i and b_i for the above equations are given in Table 1.2 [16].

Table 1.2: Coefficients for the saturation equations from Oldenbourg

Index i	a_i	b_i
1	-7.85823	1.99206
2	1.83991	1.10123
3	-11.7811	-0.512506
4	22.6705	-1.75263
5	-15.9393	-45.4485
6	1.77516	-6.75615×10^5

The enthalpy of the liquid phase (water) is calculated from its departure from water vapor state enthalpy as [15]:

$$h_l - h_{g,1} = (C_{v,l} - C_{v,g})(T - T_0) - h_{lh} + \frac{p}{\rho_l} - \frac{\mathcal{R}}{W_{g,1}}T \tag{1.63}$$

where $h_{g,1}$ is the enthalpy of gas species 1 (water vapor), $W_{g,1}$ is the molecular weight of water vapor, and h_{lh} represents the latent heat of water vapor. The constants used to determine the enthalpy of liquid water are listed in Table 1.3.

Table 1.3: Constants for enthalpy departure of liquid water

Constant	Value
$C_{v,l}$	4180.0 J/kg K
$C_{v,g}$	1410.8 J/kg K
T_0	273.15 K
h_{lh}	2502789.4 J/kg

The viscosity and thermal conductivity of liquid phase (water) are calculated from following equations [17]:

$$\mu_l = \exp\left[c_1 + \frac{c_2}{c_3 - T}\right], \tag{1.64}$$

$$\lambda_l = d_1 + d_2 T + d_3 T^2, \tag{1.65}$$

where c_i and d_i are coefficients listed in Table 1.4 [17].

Table 1.4: Coefficients for transport quantities of liquid water

Index i	c_i	d_i
1	-10.4349	-0.7676
2	-507.881	7.5390×10^{-3}
3	149.390	-9.8250×10^{-6}

1.3.4 Phasic Mixing Rules

The fluid in the aerated-liquid injector simulation is treated as a mixture of liquid and gas. This subsection indicates equations used to determine mixture values for various thermodynamic and transport quantities.

Recall that the bulk density of mixture is defined in Equation 1.5. In order to relate it to the phasic mass fractions and densities, the bulk density is rewritten as:

$$\frac{1}{\rho} = \frac{Y_g}{\rho_g} + \frac{Y_l}{\rho_l} \tag{1.66}$$

The mixture enthalpy per unit mass, the mixture viscosity, and the mixture thermal conductivity are defined as:

$$h = Y_g h_g + Y_l h_l, \tag{1.67}$$

$$\mu = \alpha_g \mu_g + \alpha_l \mu_l, \tag{1.68}$$

$$\lambda = \alpha_g \lambda_g + \alpha_l \lambda_l, \tag{1.69}$$

where Y_l, α_g, and α_l are calculated from Y_g as follows,

$$Y_l = 1 - Y_g, \quad \alpha_g = \frac{\rho Y_g}{\rho_g}, \quad \alpha_l = 1 - \alpha_g, \tag{1.70}$$

The sound speed for the mixture, derived in Appendix A, is a function of thermodynamic derivatives, such as ρ_T, ρ_p, h_T and h_p:

$$a = \sqrt{\frac{\rho h_T}{\rho \rho_p h_T - \rho \rho_T h_p + \rho_T}} \tag{1.71}$$

These thermodynamic derivatives can be obtained by differentiating Equation 1.66 and 1.67 with respect to p and T:

$$\rho_p = \rho^2 \left(\frac{Y_g}{{\rho_g}^2} \frac{\partial \rho_g}{\partial p} + \frac{1 - Y_g}{{\rho_l}^2} \frac{\partial \rho_l}{\partial p} \right), \tag{1.72}$$

$$\rho_T = \rho^2 \left(\frac{Y_g}{{\rho_g}^2} \frac{\partial \rho_g}{\partial T} + \frac{1 - Y_g}{{\rho_l}^2} \frac{\partial \rho_l}{\partial T} \right), \tag{1.73}$$

$$h_p = (1 - Y_g) \frac{\partial h_l}{\partial p}, \tag{1.74}$$

$$h_T = Y_g \frac{\partial h_g}{\partial T} + (1 - Y_g) \frac{\partial h_l}{\partial T}, \tag{1.75}$$

1.4 Interface Surface Tension

Fluid interfacial motion induced by surface tension plays a fundamental role in many natural and industrial phenomena. Detailed analyses of these processes involve the use of numerical models to aid in understanding the resulting nonlinear fluid flows. The continuum surface force (CSF) model developed by Brackbill, *et al.* [18] is selected in

this study. This model alleviates the interface topology constraints suffered by other methods. The model interprets surface tension as a continuous, three-dimensional effect across an interface, rather than as a boundary value condition on the interface.

In the CSF model, the surface volume force, $\mathbf{F}_{\text{sv}}(\mathbf{x})$, for finite interfacial thickness, h, is expressed as

$$\mathbf{F}_{\text{sv}}(\mathbf{x}_{\text{s}}) = \sigma\kappa(\mathbf{x})\frac{\nabla\tilde{c}(\mathbf{x})}{[\,c\,]}. \tag{1.76}$$

where σ is the surface tension coefficient, κ is the interface curvature, and c is a mollified color function. σ is chosen to be 0.072 in the current work. The curvature, κ is calculated from

$$\kappa = -(\nabla \cdot \hat{n}), \tag{1.77}$$

and the normals are gradients of the mollified color function,

$$\mathbf{n}(\mathbf{x}) = \nabla\tilde{c}(\mathbf{x}). \tag{1.78}$$

The unit normal is thus

$$\hat{n}(\mathbf{x}) = \frac{\nabla\tilde{c}(\mathbf{x})}{|\nabla\tilde{c}(\mathbf{x})|}. \tag{1.79}$$

Since $\nabla\tilde{c}$ is nonzero only in the interface transition region, the surface volume force also is nonzero only in the transition region. In this work, the color function $\tilde{c}$ is chosen as volume fraction of the gas phase, α_g. Thus, $[\,c\,] = [\,\alpha_g\,] = 1.0$, and Equation 1.76 is rewritten as:

$$\mathbf{F}_{\text{sv}}(\mathbf{x}_{\text{s}}) \;=\; -\sigma\left[\nabla\cdot\left(\frac{\nabla\alpha_g}{|\nabla\alpha_g|}\right)\right]\nabla\alpha_g. \tag{1.80}$$

The surface tension force can be expressed in index notation as:

$$\mathrm{F}_{sv,x_i} = -\sigma\left[\frac{\partial}{\partial x_i}\left(\frac{\dfrac{\partial\alpha_g}{\partial x_i}}{\sqrt{\dfrac{\partial\alpha_g}{\partial x_k}\dfrac{\partial\alpha_g}{\partial x_k}}}\right)\right]\frac{\partial\alpha_g}{\partial x_i}, \tag{1.81}$$

where the derivatives are calculated in generalized coordinates in the code. Using the chain rule expressed in Equation 1.38, Equation 1.81 is transformed to generalized coordinates, and written as:

$$\mathrm{F}_{sv,\xi_i} = -\,\sigma\,\frac{\partial \xi_j}{\partial x_i}\frac{\partial}{\partial \xi_j}\left[\frac{\dfrac{\partial \xi_j}{\partial x_i}\dfrac{\partial \alpha_g}{\partial \xi_j}}{\sqrt{\left(\dfrac{\partial \xi_j}{\partial x_k}\dfrac{\partial \alpha_g}{\partial \xi_j}\right)\left(\dfrac{\partial \xi_j}{\partial x_k}\dfrac{\partial \alpha_g}{\partial \xi_j}\right)}}\right]\frac{\partial \xi_j}{\partial x_i}\frac{\partial \alpha_g}{\partial \xi_j}, \tag{1.82}$$

where x_i represents the Cartesian coordinate x, y, or z, and ξ_i represents the generalized coordinate ξ, η, or ζ.

Surface tension modeled with the CSF model eliminates the need for detailed interface information, so restrictions on the number, complexity, or dynamic evolution of interfaces having surface tension are not imposed.

2 Numerical Formulation

In this section, some algorithms required for efficient solution of the Navier-Stokes equations are presented. These methods include a time-derivative preconditioning method, a low-diffusion upwinding differencing method, discretization method, and numerical solution of the non-linear system formed.

2.1 Time-Derivative Preconditioning

The concept of time-derivative preconditioning [2, 3, 4, 5, 6, 7, 8] is now widely used to enable standard compressible gas codes to operate at very low Mach numbers. One concern with the use of time-derivative preconditioning is its lack of robustness in many situations (i.e., low speed reactive flows), which may sometimes require the use of implicit methods for time advancement. Another concern is that it needs to specify, in general, a "reference velocity" to avoid numerical difficulties in stagnation regions [10]. The system described in section 1.2.2 may be preconditioned as follows:

$$\frac{1}{J}\left(\mathbf{P}\frac{\partial \mathbf{V}}{\partial \tau}+\frac{\partial \mathbf{U}}{\partial t}\right)+\frac{\partial(\mathbf{E}-\mathbf{E_v})}{\partial \xi}+\frac{\partial(\mathbf{F}-\mathbf{F_v})}{\partial \eta}+\frac{\partial(\mathbf{G}-\mathbf{G_v})}{\partial \zeta}=\mathbf{S} \tag{2.1}$$

where $\mathbf{P}$ is a preconditioning matrix, $\mathbf{V}$ is a vector of primitive variables, which in the current work is chosen as:

$$\mathbf{V}=\begin{bmatrix} Y_{g,1} \\ \vdots \\ Y_{g,N_g-1} \\ Y_g \\ p \\ u \\ v \\ w \\ T \\ Y_{l,1} \\ \vdots \\ Y_{l,N_l-1} \end{bmatrix}, \tag{2.2}$$

τ is the time-marching variable that is used for sub-iterative purposes, and t is the physical time variable used for unsteady computations. In order to distinguish τ from the physical time variable t, we refer to terms involving τ as pseudo-time derivatives.

For steady-state computations, Equation 2.1 will contain only the pseudo-time derivatives and the solution is marched in pseudo time until the desired steady state is attained. For unsteady computations, Equation 2.1 will contain both pseudo- and physical time derivatives. In that case, the transient solution is advanced in physical time and, at each physical time step, pseudo-time iterations are performed until the non-linear equations are satisfied. This strategy is commonly referred to as dual time stepping [6, 8].

The preconditioning matrix used in the current work is that of Weiss and Smith [4], which is a variant of the Turkel [2, 5] and Choi-Merkle [3] preconditioners. This preconditioner may be expressed as a rank-one perturbation of the Jacobian matrix $\frac{\partial \mathbf{U}}{\partial \mathbf{V}}$:

$$\mathbf{P} = \frac{\partial \mathbf{U}}{\partial \mathbf{V}} + \Theta \vec{u}\vec{v}^T \tag{2.3}$$

where

$$\vec{u} = \begin{bmatrix} Y_{g,1} \\ \vdots \\ Y_{g,N_g-1} \\ Y_g \\ 1 \\ u \\ v \\ w \\ H \\ Y_{l,1} \\ \vdots \\ Y_{l,N_l-1} \end{bmatrix}, \quad \vec{v} = \frac{\partial p}{\partial \mathbf{V}} = \begin{bmatrix} \partial p / \partial Y_{g,1} \\ \vdots \\ \partial p / \partial Y_{g,N_g-1} \\ \partial p / \partial Y_g \\ \partial p / \partial p \\ \partial p / \partial u \\ \partial p / \partial v \\ \partial p / \partial w \\ \partial p / \partial T \\ \partial p / \partial Y_{l,1} \\ \vdots \\ \partial p / \partial Y_{l,N_l-1} \end{bmatrix} = \begin{bmatrix} 0 \\ \vdots \\ 0 \\ 0 \\ 1 \\ 0 \\ 0 \\ 0 \\ 0 \\ 0 \\ \vdots \\ 0 \end{bmatrix}, \tag{2.4}$$

$$\Theta = \frac{1}{V_{ref}^2} - \frac{1}{a^2}, \tag{2.5}$$

and V_{ref}^2 is a suitably defined reference velocity. The quantity a is the sound speed as defined in Appendix A. In the limit of an incompressible flow ($a^2 \to \infty$), this preconditioner reduces to a variant of Chorin's artificial compressibility method [19], while $\dfrac{\partial \mathbf{U}}{\partial \mathbf{V}}$ is recovered as $V_{ref}^2 \to a^2$. The reference velocity is typically defined as

$$V_{ref}^2 = \min\left[a^2, \max\left(|\vec{V}|^2, V_\infty^2\right)\right], \tag{2.6}$$

where $|\vec{V}|$ is the local fluid velocity magnitude, and V_∞ is a user defined cutoff velocity, which is designed to prevent singular behavior in stagnation regions. As shown in References 7, 10, 20 and 21, this choice may be not adequate for low speed unsteady flows at small physical time steps. Another choice of the reference velocity for unsteady preconditioning is defined as

$$V_{ref,un}^2 = \min\left[a^2, \max\left(|\vec{V}|^2, V_\infty^2, \left(\frac{\sqrt{\Delta x_i^2}}{\Delta t}\right)^2\right)\right], \tag{2.7}$$

where $\sqrt{\Delta x_i^2}$ is a length scale characteristic of a mesh point. In the following sections, different choices for the reference velocity will be used in the implementations of flux-splitting and time integration, and their effects on spatial and temporal accuracy will be investigated.

According to Appendix C, the eigenvalues of the flux Jacobian in ξ direction, $\mathbf{P}^{-1}\dfrac{\partial \mathbf{E}}{\partial \mathbf{V}}$, are $\overline{U}$ and $\overline{U}' \pm a'$, where $\overline{U}$ is the normalized contravariant velocity component in the ξ direction,

$$\overline{U} = \frac{1}{|\nabla \xi|}\left(\xi_x u + \xi_y v + \xi_z w\right), \tag{2.8}$$

$$\overline{U}' \pm a' = \frac{1 + M_{ref}^2}{2}\left[\overline{U} \pm a\frac{\sqrt{\left(1 - M_{ref}^2\right)^2 M^2 + 4M_{ref}^2}}{1 + M_{ref}^2}\right], \tag{2.9}$$

where

$$M_{ref} = \frac{V_{ref,un}}{a}, \quad M = \frac{\overline{U}}{a}, \tag{2.10}$$

are the reference Mach number and the Mach number. The reference Mach number, M_{ref}, enables the flux splitting scheme to revert to its original formulations for $M > 1$. In the limit of an incompressible flow, the acoustic eigenvalues revert to

$$\overline{U}' \pm a' = \frac{1}{2}\left(\overline{U} \pm a\sqrt{M^2 + 4M_{ref}^2}\right), \tag{2.11}$$

which now scale as the reference velocity.

2.2 Discrete Representation

The governing equations are solved using a cell-centered, generalized coordinate finite volume discretization. Associating the i index with the ξ coordinate, the j index with the η coordinate, and the k index with the ζ coordinate, the discrete representation of the governing equations given in Equation 1.39 is then expressed as:

$$\begin{aligned}\frac{\partial \mathbf{U}_{i,j,k}}{\partial t} &+ \frac{(\mathbf{E}-\mathbf{E_v})_{i+\frac{1}{2},j,k} - (\mathbf{E}-\mathbf{E_v})_{i-\frac{1}{2},j,k}}{\Delta\xi} \\ &+ \frac{(\mathbf{F}-\mathbf{F_v})_{i,j+\frac{1}{2},k} - (\mathbf{F}-\mathbf{F_v})_{i,j-\frac{1}{2},k}}{\Delta\eta} \\ &+ \frac{(\mathbf{G}-\mathbf{G_v})_{i,j,k+\frac{1}{2}} - (\mathbf{G}-\mathbf{G_v})_{i,j,k-\frac{1}{2}}}{\Delta\zeta} \\ &- \mathbf{S}_{i,j,k} = 0,\end{aligned} \tag{2.12}$$

where $\Delta\xi$, $\Delta\eta$, and $\Delta\zeta$ are assumed to be unity for convenience. An equivalent form of Equation 2.12, useful in formulating time integration methods, is written as:

$$\frac{\partial \mathbf{U}_{i,j,k}}{\partial t} = -R_{i,j,k} \tag{2.13}$$

where

$$\begin{aligned}R_{i,j,k} &= \frac{(\mathbf{E}-\mathbf{E_v})_{i+\frac{1}{2},j,k} - (\mathbf{E}-\mathbf{E_v})_{i-\frac{1}{2},j,k}}{\Delta\xi} + \frac{(\mathbf{F}-\mathbf{F_v})_{i,j+\frac{1}{2},k} - (\mathbf{F}-\mathbf{F_v})_{i,j-\frac{1}{2},k}}{\Delta\eta} \\ &+ \frac{(\mathbf{G}-\mathbf{G_v})_{i,j,k+\frac{1}{2}} - (\mathbf{G}-\mathbf{G_v})_{i,j,k-\frac{1}{2}}}{\Delta\zeta} - \mathbf{S}_{i,j,k}\end{aligned} \tag{2.14}$$

is the residual vector that represents the "steady" part of governing equation system at grid point (i, j, k).

2.3 Flux-Splitting Scheme

A recent trend in the development of upwind schemes has been the construction of hybrid flux-vector/flux-difference splitting schemes that attempt to combine high resolution with efficiency and compactness of formulation. This class of schemes may be referred to generally as the 'AUSM-family' [22, 23], with AUSM standing for Advective Upwind Splitting Method, the first successful approach of this type. One such method, the low-diffusion flux-splitting scheme (LDFSS) of Edwards [9, 10], is employed in the current study to discretize the inviscid fluxes in the governing equations, while the viscous and diffusive terms are discretized using central differences.

2.3.1 LDFSS

The LDFSS provides accurate resolution of stationary and moving contact discontinuities while preserving monotonicity of solution and satisfying entropy condition. Details regarding the original development of LDFSS may be found in References 9 and 24. The algorithm is formulated as an upwinding procedure in one dimension, and then applied to three spatial dimensions. For generality, the derivation that follows is for the ξ direction flux only.

A key in the extension of LDFSS to operate as a more "universal" flux-splitting is the use of a "numerical speed of sound" [20, 21, 25] derived from the acoustic eigenvalues of the preconditioned system and evaluated at a cell interface:

$$\tilde{a}_{\frac{1}{2}} = \left[\frac{\sqrt{\left(1 - M_{ref}^2\right)^2 \overline{\mathcal{U}}^2 + 4V_{ref,un}^2}}{1 + M_{ref}^2} \right]_{\frac{1}{2}}, \tag{2.15}$$

where the '$\frac{1}{2}$' notation indicates the evaluation of Equation 2.15 using cell-averaged velocity and sound speed data, and M_{ref} is the reference Mach number as defined in Equation 2.10. Different forms for this averaged sound speed can be used, and results can be affected by the choice. The present work utilizes arithmetic averaging

exclusively:

$$a_{\frac{1}{2}} = \frac{1}{2}\left(a_L + a_R\right) \tag{2.16}$$

Other quantities needed in the formulation are Mach numbers at left and right states, and van Leer/Liou polynomials in Mach number [26]:

$$M_{L,R} = \frac{\overline{\mathcal{U}}_{L,R}}{\tilde{a}_{\frac{1}{2}}} \tag{2.17}$$

$$M^{\pm}_{(1)} = \frac{1}{2}\left(M \pm |M|\right), \tag{2.18}$$

$$M^{\pm}_{(2)} = \begin{cases} \pm\frac{1}{4}\left(M \pm 1\right)^2, & |M| < 1, \\ M^{\pm}_{(1)}, & \text{otherwise}, \end{cases} \tag{2.19}$$

The properties at the left (L) and right (R) states used in the above definitions will be specified later in Section 2.3.2.

Given these basic definitions, the inviscid ξ direction flux $\mathbf{E}$ can be split into convective and pressure contributions:

$$\mathbf{E} = \mathbf{E}^c + \mathbf{E}^p = \frac{|\nabla\xi|}{J}\left(\overline{\mathcal{U}}\Phi + p\Psi\right) \tag{2.20}$$

where

$$\Phi = \begin{bmatrix} \rho Y_{V,1} Y_V \\ \vdots \\ \rho Y_{V,N_V-1} Y_V \\ \rho Y_V \\ \rho \\ \rho u \\ \rho v \\ \rho w \\ \rho H \\ \rho Y_{L,1} Y_L \\ \vdots \\ \rho Y_{L,N_L-1} Y_L \end{bmatrix}, \quad \Psi = \begin{bmatrix} 0 \\ \vdots \\ 0 \\ 0 \\ 0 \\ \overline{\xi}_x \\ \overline{\xi}_y \\ \overline{\xi}_z \\ 0 \\ 0 \\ \vdots \\ 0 \end{bmatrix}, \tag{2.21}$$

$$\overline{\xi}_x = \frac{\xi_x}{|\nabla\xi|}, \quad \overline{\xi}_y = \frac{\xi_y}{|\nabla\xi|}, \quad \overline{\xi}_z = \frac{\xi_z}{|\nabla\xi|}, \tag{2.22}$$

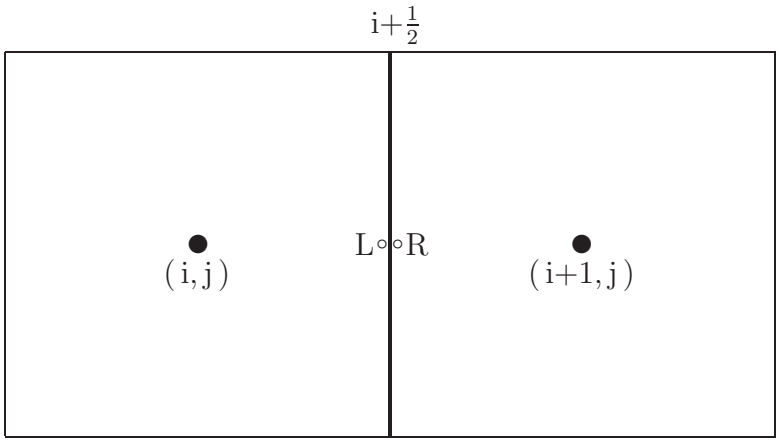

Figure 2.1: Upwinding stencil used for LDFSS algorithm (ξ direction).

Figure 2.1 shows the computational stencil used in this work. The upwinding scheme is performed at the cell interfaces, denoted by the $i+\frac{1}{2}$ tab in Figure 2.1, using the properties at the left (L) and right (R) states. The LDFSS scheme applied to the cell interfaces results in the inviscid flux being split into convective and pressure parts as the sum of left and right components:

$$\begin{aligned} \mathbf{E}_{i+\frac{1}{2}} &= \mathbf{E}^c_{i+\frac{1}{2}} + \mathbf{E}^p_{i+\frac{1}{2}} \\ \mathbf{E}^c_{i+\frac{1}{2}} &= \frac{|\nabla\xi|}{J}\left(U^+\Phi_L + U^-\Phi_R\right) \\ \mathbf{E}^p_{i+\frac{1}{2}} &= \frac{|\nabla\xi|}{J}P_{\frac{1}{2}}\Psi_i \end{aligned} \tag{2.23}$$

where the split velocities $U^\pm$ and the interface pressure $P_{\frac{1}{2}}$ are functions of the Mach number, and are defined as

$$U^+ = \tilde{a}_{\frac{1}{2}}\left[\mathcal{M}^+ - \mathcal{M}_{\frac{1}{2}}\left(1 - \frac{p_L - p_R}{2\rho_L V^2_{ref,\frac{1}{2}}}\right)\right], \tag{2.24}$$

$$U^- = \tilde{a}_{\frac{1}{2}}\left[\mathcal{M}^- + \mathcal{M}_{\frac{1}{2}}\left(1 + \frac{p_L - p_R}{2\rho_R V^2_{ref,\frac{1}{2}}}\right)\right], \tag{2.25}$$

$$\begin{aligned} P_{\frac{1}{2}} &= \frac{1}{2}\left(p_L + p_R\right) + \frac{1}{2}\left(P^+ - P^-\right)\left(p_L - p_R\right) \\ &\quad + \rho_{\frac{1}{2}} V^2_{ref,\frac{1}{2}}\left(P^+ + P^- - 1\right), \end{aligned} \tag{2.26}$$

$$\text{where} \quad \mathcal{M}^+ = \alpha_L^+ (1+\beta_L) M_L - \beta_L M_{(2),L}^+, \tag{2.27}$$

$$\mathcal{M}^- = \alpha_R^- (1+\beta_R) M_R - \beta_R M_{(2),R}^-. \tag{2.28}$$

In the above equations, $\rho_{\frac{1}{2}}$ is the interface density, and $V_{ref,\frac{1}{2}}$ is the interface reference velocity as defined in Equation 2.6 or 2.7.The various quantities in the previous sets of equations are given as:

$$\alpha_{L,R}^{\pm} = \frac{1}{2}\left[1.0 \pm \text{sign}\left(1.0, M_{L,R}\right)\right] \tag{2.29}$$

$$\beta_{L,R} = -\max\left[0.0, 1.0 - \text{int}\left(|M_{L,R}|\right)\right] \tag{2.30}$$

$$\mathcal{M}_{\frac{1}{2}} = \frac{1}{2}\left(\mathcal{M}^+ - \alpha_L^+ M_L - \mathcal{M}^- + \alpha_R^- M_R\right) \tag{2.31}$$

$$P^{\pm} = \alpha_{L,R}^{\pm}\left(1+\beta_{L,R}\right) - \frac{\beta_{L,R}}{2}\left[1.0 \pm g\left(M_{L,R}\right)\right], \tag{2.32}$$

where $g(M)$ is a γ-polynomial proposed by Liou [22, 26]:

$$g(M) = \begin{cases} M, & \text{in first degree, or} \\ \left(\frac{3}{2}+2\gamma\right)M - \left(\frac{1}{2}+4\gamma\right)M^3 + 2\gamma M^5, & \\ & \text{in third degree if } \gamma = 0 \text{ or fifth degree if } \gamma \neq 0, \end{cases} \tag{2.33}$$

In the current work, $g(M)$ is chosen to be in first degree.

As discussed later, different reference velocities may be used in the developments of Equations 2.24-2.26. For the split velocities $U^{\pm}$, the unsteady reference velocity as defined in Equation 2.7 is used for most calculations. For the interface pressure $P_{\frac{1}{2}}$, the steady reference velocity (Equation 2.6) is used for most calculations. Note that these choices require different expressions for $\tilde{a}_{\frac{1}{2}}$ and $M_{L,R}$, in addition to $V_{ref,\frac{1}{2}}^2$.

2.3.2 Second-Order Scheme

The LDFSS is extended to second order to improve the accuracy of the solution. The second order extension is accomplished by a slope-limited, upwind-biased interpolation of the primitive variable vector, $\mathbf{V}$, to the cell interface, using essentially non-oscillatory [27, 28] (ENO) interpolation techniques or TVD-type methods. A

TVD-type van Albada scheme [29, 30] is used to get left and right interpolations in this study. This approach can be described as follows.

We choose q to be an arbitrary quantity which will be interpolated to the left and right states. Then the interpolations can be expressed as:

$$q_L = q_i + P_i^l \cdot \text{avg}\left(q_{i+1} - q_i, q_i - q_{i-1}\right), \tag{2.34}$$

$$q_R = q_{i+1} - P_{i+1}^l \cdot \text{avg}\left(q_{i+2} - q_{i+1}, q_{i+1} - q_i\right), \tag{2.35}$$

where P^l is a pressure limiter and $\text{avg}(a, b)$ is an averaging procedure.

The pressure limiter P_i^l is defined as:

$$P_i^l = \frac{1}{2}\left[1.0 - \max\left(\frac{|(\delta p)_i|}{|(\delta p)_i| + \kappa_0 p_\infty}, \frac{|(\delta \alpha_g)_i|}{|(\delta \alpha_g)_i| + 10.0\kappa_0}\right)\right], \tag{2.36}$$

$$\text{and} \qquad (\delta p)_i = p_{i+1} - p_{i-1}, \quad (\delta \alpha_g)_i = (\alpha_g)_{i+1} - (\alpha_g)_{i-1}, \tag{2.37}$$

where κ_0 is a constant, and p_∞ is the freestream pressure.

The function $\text{avg}(a, b)$ is defined as in Reference 29:

$$\text{avg}(a, b) = \frac{(b^2 + \epsilon_q)a + (a^2 + \epsilon_q)b}{a^2 + b^2 + 2\epsilon_q}, \tag{2.38}$$

where ϵ_q is a constant factor for q.

2.4 Time Advancement

A dual time stepping [6] method based on a lower-upper symmetric planar Gauss-Seidel (LU-SPGS) partitioning of the system Jacobian matrix [31, 32] is used with implicit source terms as a means of solving the three-dimensional form of the governing equations. This method provides simultaneous solution of $(N_V + N_L - 2)$ species continuity equations, one phasic continuity equation, one mixture continuity equation, three mixture momentum equations, one mixture energy equation, and two transport equations for the turbulence kinetic energy (k) and turbulence frequency (ω). The latter two equations are included for use in future calculations but no turbulence

modeling is employed in this study. The following dual time stepping procedure is performed to obtain the correction $\Delta\mathbf{V}^{n+1,\mathrm{k}+1}$, where $n+1$ represents the physical time level, and $\mathrm{k}+1$ represents the pseudo time level.

Firstly, the residual of the unsteady form of the governing equation set at physical time level $n+1$, pseudo time level k is defined using following discretization:

$$\mathbf{R}^{n+1,\mathrm{k}} = \frac{3\mathbf{U}^{n+1,\mathrm{k}} - 4\mathbf{U}^{n} + \mathbf{U}^{n-1}}{2\Delta t} + R\left(\mathbf{U}^{n+1,\mathrm{k}}\right). \tag{2.39}$$

In this equation, $\mathbf{U}^{n+1,\mathrm{k}}$ is the conservative variable vector at physical time level $n+1$, pseudo time level k; $\mathbf{U}^{n}$ is the conservative variable vector at physical time level n; $\mathbf{U}^{n-1}$ is the conservative variable vector at physical time level $n-1$; $R\left(\mathbf{U}^{n+1,\mathrm{k}}\right)$ is the discrete representation of the steady part of the governing equation set (see Equation 2.14) at physical time level $n+1$, pseudo time level k.

Secondly, the update vector in primitive variables, $\Delta\mathbf{V}^{n+1,\mathrm{k}+1}$, is solved in a large, sparse linear system, which is obtained by discretizing the preconditioned system using a backward Euler time linearization. This procedure is expressed as:

$$\begin{aligned}
&\left[\frac{\mathbf{P}}{\Delta\tau} + \frac{1}{\Delta t}\frac{\partial\mathbf{U}}{\partial\mathbf{V}} + A - \frac{\partial\mathbf{S}}{\partial\mathbf{V}}\right]^{n+1,\mathrm{k}}_{i,j,k} \Delta\mathbf{V}^{n+1,\mathrm{k}+1}_{i,j,k} \\
&+ B^{n+1,\mathrm{k}}_{i,j,k}\Delta\mathbf{V}^{n+1,\mathrm{k}+1}_{i,j-1,k} + C^{n+1,\mathrm{k}}_{i,j,k}\Delta\mathbf{V}^{n+1,\mathrm{k}+1}_{i,j+1,k} \\
&+ D^{n+1,\mathrm{k}}_{i,j,k}\Delta\mathbf{V}^{n+1,\mathrm{k}+1}_{i,j,k-1} + E^{n+1,\mathrm{k}}_{i,j,k}\Delta\mathbf{V}^{n+1,\mathrm{k}+1}_{i,j,k+1} \\
&+ F^{n+1,\mathrm{k}}_{i,j,k}\Delta\mathbf{V}^{n+1,\mathrm{k}+1}_{i-1,j,k} + G^{n+1,\mathrm{k}}_{i,j,k}\Delta\mathbf{V}^{n+1,\mathrm{k}+1}_{i+1,j,k} \\
&= -\mathbf{R}^{n+1,\mathrm{k}}_{i,j,k}
\end{aligned} \tag{2.40}$$

where $\Delta\tau$ is the pseudo-time step, Δt is the physical time step, $\mathbf{R}$ is the residual vector obtained from Equation 2.39, and the matrices A-G are functions of the inviscid and viscous flux Jacobians, constructed as outlined in Appendix C and Reference 9. The basic implicit operator is formed by ordering Equation 2.40 over the mesh nodes and incorporating implicit representations for the boundary conditions [33]. The resulting

system Jacobian matrix is denoted as $\mathbf{A}$. Thus, Equation 2.40 can be written as:

$$\mathbf{A}\Delta\mathbf{V}^{n+1,\mathrm{k}+1} = \left(\mathscr{L} + \mathscr{D} + \mathscr{U}\right)\Delta\mathbf{V}^{n+1,\mathrm{k}+1} = -\mathbf{R}_{i,j,k}^{n+1,\mathrm{k}} \tag{2.41}$$

where $\mathscr{L}$ contains the portions of $\mathbf{A}$ below the block diagonal of $\mathbf{A}$, $\mathscr{D}$ is the block diagonal of $\mathbf{A}$, and $\mathscr{U}$ is the upper part of $\mathbf{A}$. Specifically, $\mathscr{L}$, $\mathscr{U}$, and $\mathscr{D}$ are

$$\begin{aligned} \mathscr{L} &= F, \\ \mathscr{U} &= G, \\ \mathscr{D} &= P + B + C + D + E, \\ \text{where} \quad P &= \frac{\mathbf{P}}{\Delta\tau} + \frac{1}{\Delta t}\frac{\partial \mathbf{U}}{\partial \mathbf{V}} + A - \frac{\partial \mathbf{S}}{\partial \mathbf{V}}. \end{aligned} \tag{2.42}$$

Then, matrix $\mathbf{A}$ is approximated by $\mathbf{M}$ using SPGS partitioning as:

$$\mathbf{M} = \left(\mathscr{D} + \mathscr{L}\right)\left(\mathscr{D}\right)^{-1}\left(\mathscr{D} + \mathscr{U}\right), \tag{2.43}$$

and Equation 2.41 is approximately factored as:

$$\left(\mathscr{D} + \mathscr{L}\right)^{n+1,\mathrm{k}}\left(\mathscr{D}^{n+1,\mathrm{k}}\right)^{-1}\left(\mathscr{D} + \mathscr{U}\right)^{n+1,\mathrm{k}}\Delta\mathbf{V}^{n+1,\mathrm{k}+1} = -\mathbf{R}^{n+1,\mathrm{k}}. \tag{2.44}$$

The SPGS partitioning is an approximation to the matrix $\mathbf{A}$, with factorization error $\mathscr{L}\mathscr{D}^{-1}\mathscr{U}\Delta\mathbf{V}$. This algorithm is implemented in two steps, a forward and backward step in ξ direction as follows:

$$\text{step 1} \quad : \quad \Delta\mathbf{V}_i^{n+1,\mathrm{k}+\frac{1}{2}} = \left(\mathscr{D}_i^{n+1,\mathrm{k}}\right)^{-1}\left[-\mathbf{R}_i^{n+1,\mathrm{k}} - \mathscr{L}_{i-1}^{n+1,\mathrm{k}}\Delta\mathbf{V}_{i-1}^{n+1,\mathrm{k}+\frac{1}{2}}\right], \tag{2.45}$$

$$\text{step 2} \quad : \quad \Delta\mathbf{V}_i^{n+1,\mathrm{k}+1} = \Delta\mathbf{V}_i^{n+1,\mathrm{k}+\frac{1}{2}} - \left(\mathscr{D}_i^{n+1,\mathrm{k}}\right)^{-1}\mathscr{U}_{i+1}^{n+1,\mathrm{k}}\Delta\mathbf{V}_{i+1}^{n+1,\mathrm{k}+1}. \tag{2.46}$$

At each ξ direction, the inversion of the block pentadiagonal matrix $\mathscr{D}_i$ is solved using an incomplete LU (ILU) approximate factorization algorithm. A correction scheme is used to help correct the update vector of the primitive variable as:

$$\Delta\mathbf{V}_{correction}^{n+1,\mathrm{k}+1} = \Delta\mathbf{V}^{n+1,\mathrm{k}+1} - \mathbf{M}^{-1}\mathbf{A}\Delta\mathbf{V}^{n+1,\mathrm{k}+1}. \tag{2.47}$$

The advantage of introducing this procedure is that it implicitly couples the solution across block boundaries, thus allowing a more rapid transfer of information across the domain. However, it is also more expensive since it introduces more calculations.

Finally, the primitive variable vector at the new pseudo time level k + 1 is then updated by:

$$\mathbf{V}^{n+1,\mathrm{k}+1} = \mathbf{V}^{n+1,\mathrm{k}} + \Delta\mathbf{V}^{n+1,\mathrm{k}+1}_{correction}. \tag{2.48}$$

Adequate convergence of the subiteration procedure is a necessity to maintain proper time accuracy. This is particularly important for low speed, nearly incompressible flows, as the subiteration procedure acts to enforce the discrete divergence-free condition $\frac{\partial u_i}{\partial x_i} = 0$ at each physical time step. As shown in Reference 7, it is necessary to introduce the physical time step into the reference velocity definition, Equation 2.7, which appears both in the preconditioning matrices and in the flux-splitting, in order to enable good subiteration convergence in the limit of small time steps and small Mach numbers. Results presented later indicate the effects of employing this definition on mass conservation.

3 Implementation

This section describes the fluid model, multiblock parallel approach, boundary and inlet conditions.

3.1 Flow Model

The Air Force Research Laboratory (AFRL) aerated-liquid injector configuration is simulated in the current work [1]. A rectangular aerated-liquid injector, consisting of an internal tube for aerating gas flow, is schematically illustrated in Figure 3.1.

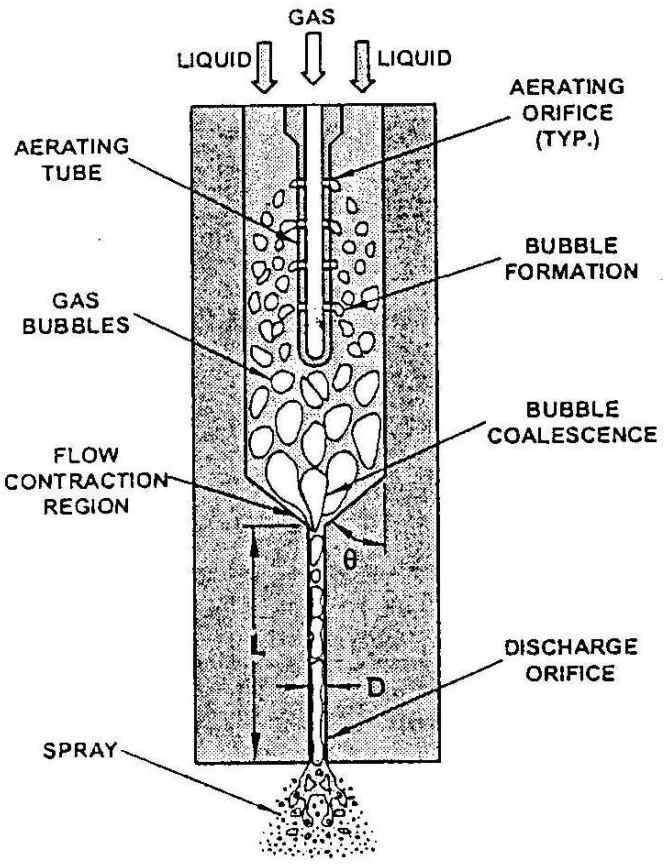

Figure 3.1: Schematic of the injector assembly and internal flow structure

Aerated-liquid jets are injected vertically downward into a quiescent environment. The rectangular configuration is with a dimension of 6.4 mm by 2.0 mm. The aerating

gas flows inside the aerating tube and then passes through small orifices in various arrangements. In the current work, the experimental Configuration V aerating tube is simulated, which is shown in Figure 3.2. This tube consists of one 760-μm orifice at the tip of the aerating tube, which is located 25.4 mm from the entrance of the final discharge passage [1]. A square cross section with dimension, D, of 2.0 mm is used for the final discharge passage. The length of the nozzle block, L, is 20D, while the converging angle is 50 degrees. Water is used as the test liquid and nitrogen is used as the aerating gas.

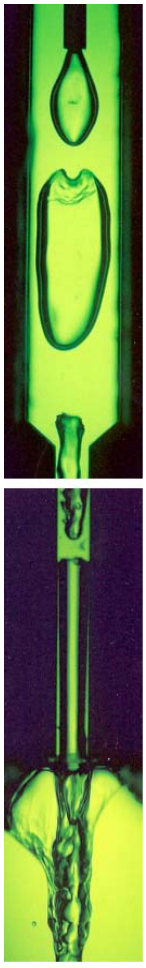

Figure 3.2: Experimental photographs of the Configuration V aerating tube and internal two-phase flow structure, $Q_L = 0.38$ l/min, $GLR = 0.08\%$

In this study, we idealize the injector to two dimensions. A simple way is to assume that the aerating tube has a rectangular cross-section other than a circular one. Thus, the aerated-liquid injector has the same length in one dimension and can be easily changed to 2-D for convenience of numerical simulations. After some calculations, we get the width of the internal aerating gas tube of the numerical model as the value of 227 μm, which is equivalent to the diameter of the experimental tube in 760 μm. This 2-D injector is 88 mm long, 6.4 mm wide in the mixing chamber and 2.0 mm wide in the discharge passage. The length of the discharge passage is 40 mm, while the converging angle is 50 degrees.

3.2 Multiblock Parallel Approach

The calculation of flows within complex domains using structured grids usually requires some type of domain decomposition strategy. Domain decomposition involves the partitioning of a complex domain into simpler subdomains, which may be solved in sequence or in parallel. The two-dimensional computational domain is investigated in this work as illustrated in Figure 3.3.

The two-dimensional computational domain is decomposed into 30 blocks as shown in Figure 3.3. Eight blocks contain 121x11x3 points, six contain 121x16x3 points, sixteen contain 121x11x3 points, for a total of 188,760 points. In order to capture viscous layer gradients, the mesh is clustered to all solid surfaces.

The calculations were parallelized with Message-Passing Interface [34, 35] standard and run on the IBM-SP at the North Carolina Supercomputing Center (NCSC).

3.3 Boundary Conditions

Subsonic inflow boundary conditions are imposed to inlet flows for both liquid and gas. There are different boundary conditions for liquid and gas. For the liquid, the properties, such as u, v, w, T, Y_g, etc., are fixed, while the pressure is extrapo-

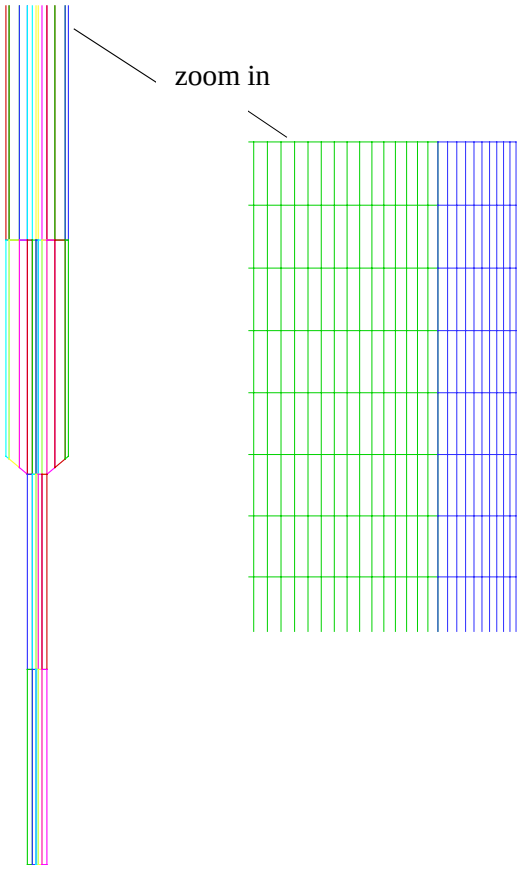

Figure 3.3: 2-D computational domain decomposition

lated from the interior of the domain by integrating the 1-D compatibility equation corresponding to the leftward-propagating pseudo-acoustic wave. A Bernoulli inflow boundary condition is also used for the liquid in one case. In the Bernoulli inflow boundary condition, some properties, such as v, w, T, Y_g, etc., and the total pressure p_0 are fixed, where p_0 can be expressed as:

$$p_0 = p_\infty + \frac{1}{2}\rho_\infty u_\infty^2 = \text{constant}. \tag{3.1}$$

Meanwhile axial velocity, u, is extrapolated from the interior of the domain. For the gas, the properties, ρu, v, w, T, Y_g, etc., are fixed, while the pressure is extrapolated from the interior of the domain.

Subsonic outflow boundary conditions were applied to the outlet flows. In the

outflow boundary, the pressure is fixed at 1 atm and the other properties are extrapolated from the interior of the domain.

No-slip and adiabatic wall boundary conditions are applied to all solid wall surfaces on the computational grids. These boundary conditions assume that there is no heat transfer through solid surfaces during the calculations of the aerating-liquid injector.

The decomposition introduces interface boundaries between adjacent blocks. The flow variables along interface boundaries in ξ and η directions are updated using adjacent interface data during the parallel transfer. In ζ direction, symmetry boundary conditions are applied.

3.4 Inlet Conditions

The inlet flow conditions and Initial Conditions for the calculations are listed in Table 3.1.

Table 3.1: Inlet flow conditions and initial conditions

Property	Value
$p_{\infty,g}$	137126.0 Pa
$p_{\infty,l}$	101325.0 Pa
T_∞	300.0 K
$u_{\infty,l}$	0.586 m/s
Y_g^{init} (for the aerating tube)	1.0
Y_g^{init} (for the liquid tank)	0.0
Y_{g,N_2}	1.0
Y_{l,H_2O}	1.0
$(\rho u)_g$ $(GLR = 0.08\%)$	11.469 kg/(m^2·s)
$(\rho u)_g$ $(GLR = 2.45\%)$	351.238 kg/(m^2·s)
U_{ref}	2.50 m/s
Δt	5.0×10^{-6} s

The pressures of gas and liquid are set to be 137126.0 Pa, and 101325.0 Pa,

respectively. The velocity of liquid is set to be 0.586 m/s. This is equivalent to the volumetric flow rate of 0.38 l/min or the mass flow rate of 6.51×10^{-3} kg/s as used in the experiments. Different conditions for $(\rho u)_g$ are imposed to the aerating tube for different GLRs. GLR stands for gas-to-liquid mass ratio. In the present study, two values of the GLRs are used: 0.08% and 2.45%.

4 Results and Discussion

We simulate the aerated-liquid injector flowfields with two gas-to-liquid (GLR) mass ratios: 0.08% and 2.45%, respectively. The volumetric flow rate of the liquid, Q_L, is set to be 0.38 l/min for each case.

4.1 $GLR = 0.08\%$ Simulations

This test case is used to assess several aspects of the numerical modeling of the injector flows. Initial values of the gas and liquid pressures are 137126.0 Pa and 101325.0 Pa, respectively. The nominal temperature is 300 K. The nominal inflow velocity of the liquid is 0.586 m/s. The mass flow rate per unit area for nitrogen gas ($(\rho u)_g$) is 11.469 kg/(m^2·s). The two-phase flow simulations were run with a fixed time step of 5.0×10^{-6} seconds, starting from an initial solution of pure water. As mentioned earlier, only two-dimensional cases are presented herein. To facilitate simulation of a two-dimensional case in the present three-dimensional code, the number of grid points in z (ξ) direction is set to 3, and symmetry boundary conditions are applied. The subiteration number is set as the value of 7 for all cases.

Figure 3.2 and Figure 4.1 present the experimental photographs of the structure of the internal two-phase flow inside the aerated-liquid injectors for $Q_L = 0.38$ l/min, $GLR = 0.08\%$. Note that these pictures were not taken at any known time interval. Also, the pictures were arranged at an assumed sequence. The formation of distinct bubbles in the mixing chamber is apparent, as is the passing of slugs of nitrogen gas into the discharge passage (see Figure 3.2 and 4.1).

4.1.1 Effects of Reference Velocity Choices and Basic Flow Features

As mentioned in Section 2, the "unsteady" preconditioning method used in this work requires specification of two reference velocities, one associated with the pressure flux

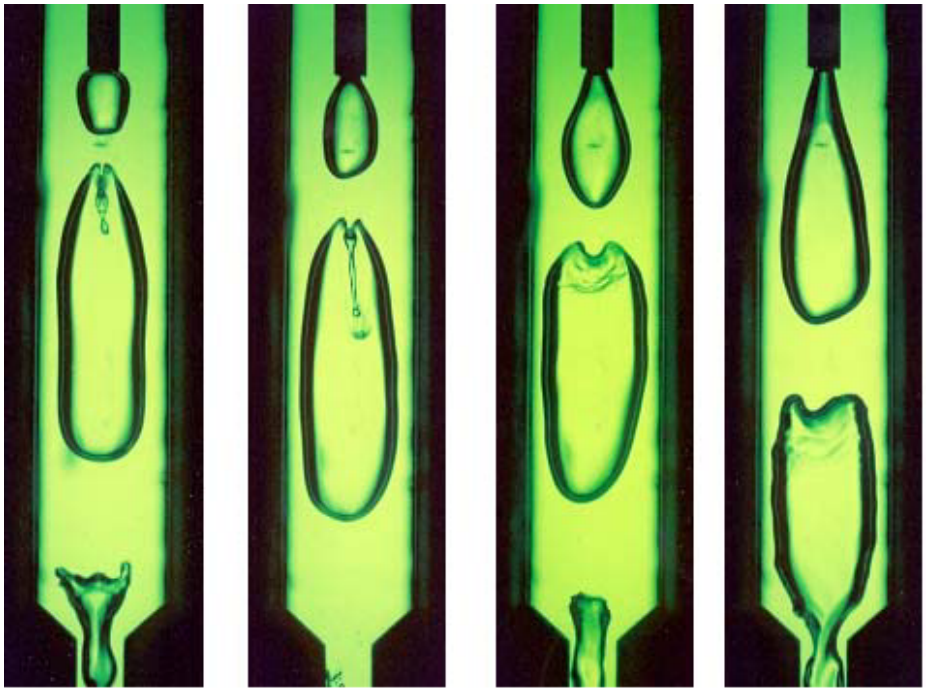

Figure 4.1: Experimental photographs for the structures of internal two-phase flows inside an aerated-liquid injector, $Q_L = 0.38$ l/min, $GLR = 0.08\%$

and the other associated with convective flux. The cases presented next illustrate the effects of different choices for these reference velocities, which are listed in Table 4.1.

Table 4.1: Different choices for the reference velocities

Case	Reference Velocities
1	V_{ref} and $V_{ref,un}$ are independent
2	$V_{ref,un} = V_{ref}$
3	$V_{ref} = V_{ref,un}$

In Case 1, the steady preconditioning reference velocity (Equation 2.6) and the unsteady preconditioning reference velocity (Equation 2.7) are used in the pressure flux and convective flux, respectively. In Case 2, the steady preconditioning reference velocity (Equation 2.6) is used in both the convective and pressure fluxes. These choices implement steady preconditioning for the whole system. In Case 3,

the unsteady preconditioning reference velocity (Equation 2.7) is used for both the convective and pressure fluxes. This procedure implements unsteady preconditioning for the whole system. For Case 1, the number of physical time iteration was 20000, equivalent to 0.10 seconds and roughly equal to one flow-through time, based on the value of Q_L. For Cases 2 and 3, the number of iterations was 10000, equivalent to 0.05 seconds.

Figure 4.2 shows gas-phase volume fraction contours for Case 1. These contour plots were extracted at a certain time interval (every 0.01 seconds or 2000 iterations).

Ten contour plots in this figure reveal the generation and the evolution of the bubbles in the mixing chamber and the discharge passage for Case 1. From the first two contour plots (t=0.01 and 0.02 seconds), we can see that the bubble evolves similarly to the experiment in its initial stages (see Figure 4.1, right two photos), but it does not break up in the mixing chamber as it does in the experiment. Rather, the bubble grows until it attaches to the downstream wall of the mixing chamber, eventually stabilizing at a fixed position and shape after about 0.03 seconds. The bubble shrinks to a thin line gradually through the converging section and starts to break up in the discharge passage as it does in the experiment (see Figure 4.1, right photo). At later time, the bubbles become less separated in the discharge passage, leading to a transition from a slugging mode to a core-annular flow pattern. The first slug of gas reaches the exit of the discharge passage at about 0.04 seconds. This will be verified later in the gas mass conservation analysis. Even though the bubble shape eventually reaches a steady state in the mixing chamber, the flowfield is still highly unsteady, characterized by the shedding of vortices from the top and bottom of the aerating tube orifice (see Figure 4.3). Most of the dynamics of the vortex shedding process takes place within the gas bubble; thus the gas-liquid interface position is not disrupted.

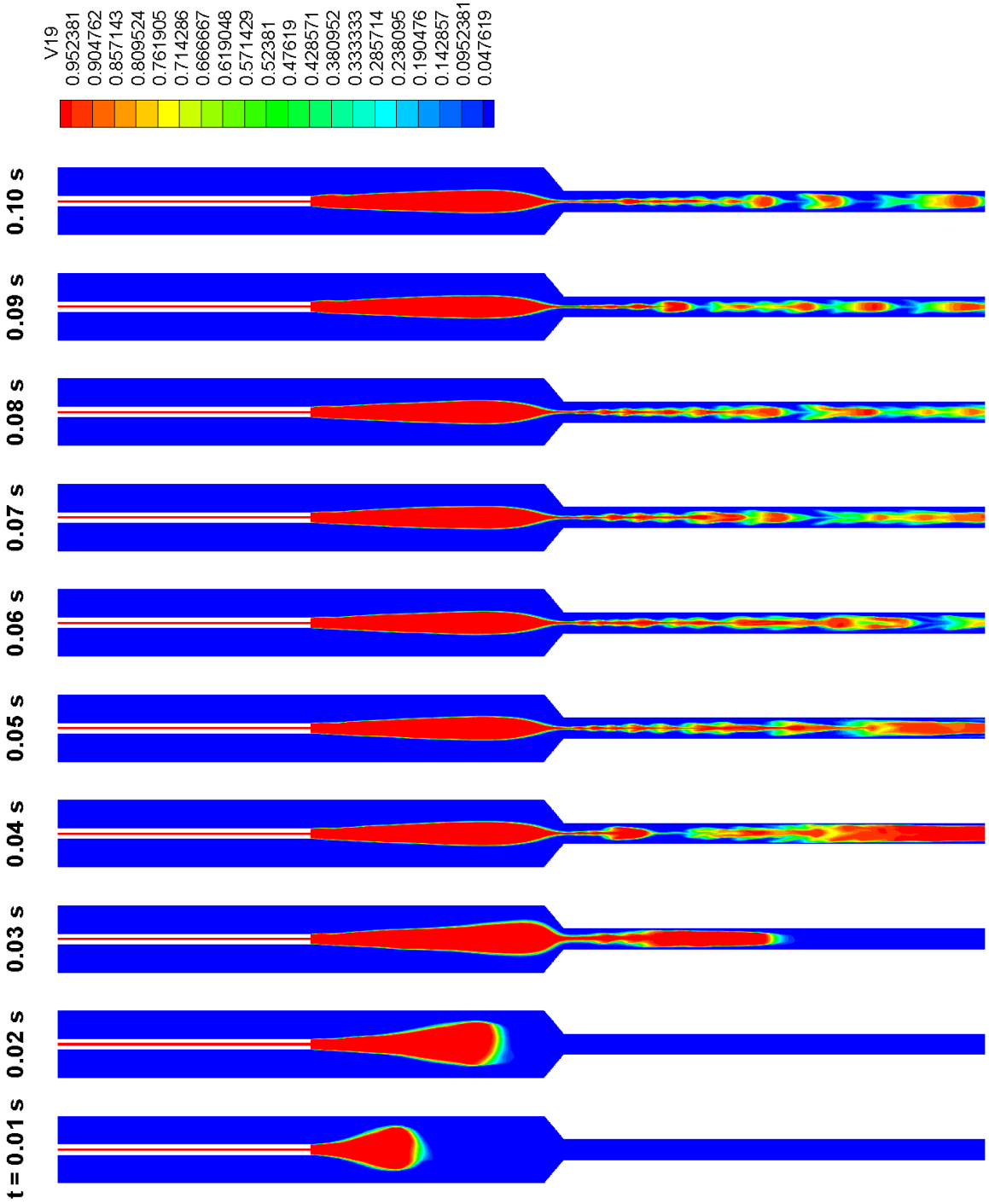

Figure 4.2: Gas-phase volume fraction contours for Case 1

Figure 4.3: Axial velocity contours for Case 1

Figure 4.3 shows axial velocity contour plots for Case 1. Comparing Figure 4.2 and Figure 4.3, we find that the higher gas void fraction region also has a higher axial velocity. This results from the high speed of inflowing gas compared with the liquid.

Figure 4.4 shows gas-phase volume fraction contours for Case 2, where the steady preconditioning reference velocity is used throughout. These contours are again extracted every 0.01 seconds.

Five contours in this figure reveal the generation and the evolution of the bubbles in the mixing chamber and the discharge passage. The initial response is very different from that of Case 1. In this case, the bubbles are generated separately in the mixing chamber in the first four contours. This is similar to the experiment except for the fact that the bubbles are not smooth and rounded as in Case 1. The bubble does not shrink to a thin line through the converging section until about 0.05 seconds (the fifth contour). From the fifth contour, we can surmise that the bubble shape in the mixing chamber will eventually stabilize, as in Case 1. But the situation in the discharge passage is a little different. The structure of the gas-liquid mixing flow in the discharge passage looks more like an core-annular flow, not like a slug/core-annular flow as in Case 1. This can be confirmed by Figure 4.5, which shows axial velocity contours for Case 2. In this figure, the core region of the discharge passage has a higher velocity, which indicates that this region is occupied mostly by aerating gas.

Figure 4.6 shows gas-phase volume fraction contours for Case 3, where the unsteady preconditioning reference velocity is used throughout. In Case 3, bubble generation is very similar to that of Case 1. In this case, the bubble does not break up in the mixing chamber and shrinks to a thin line gradually through the converging section after about 0.03 seconds (the third contour). But the situation in the discharge passage is like that of Case 2. The structure of the gas-liquid mixing flow in the

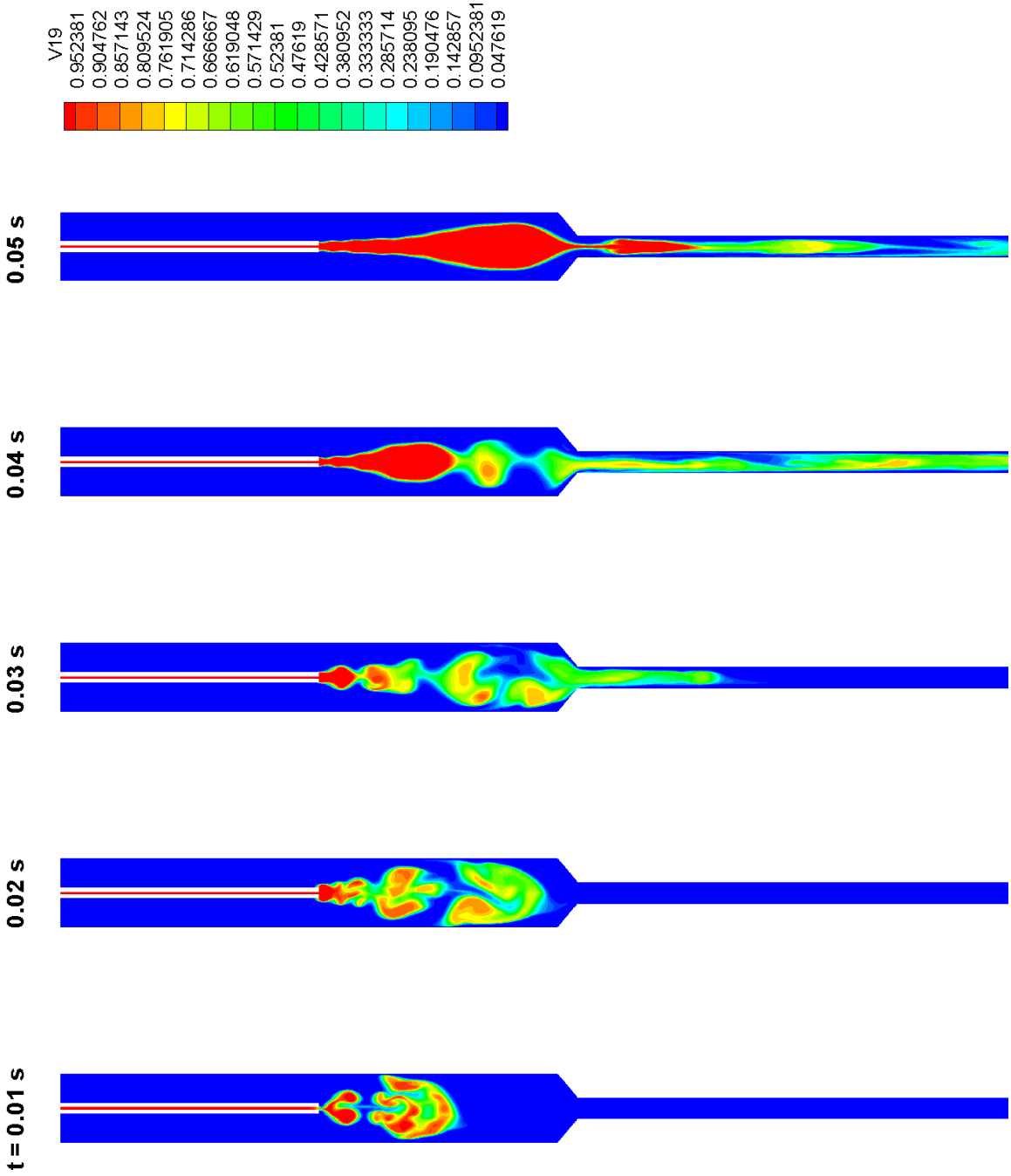

Figure 4.4: Gas-phase volume fraction contours for Case 2, $V_{ref,un} = V_{ref}$

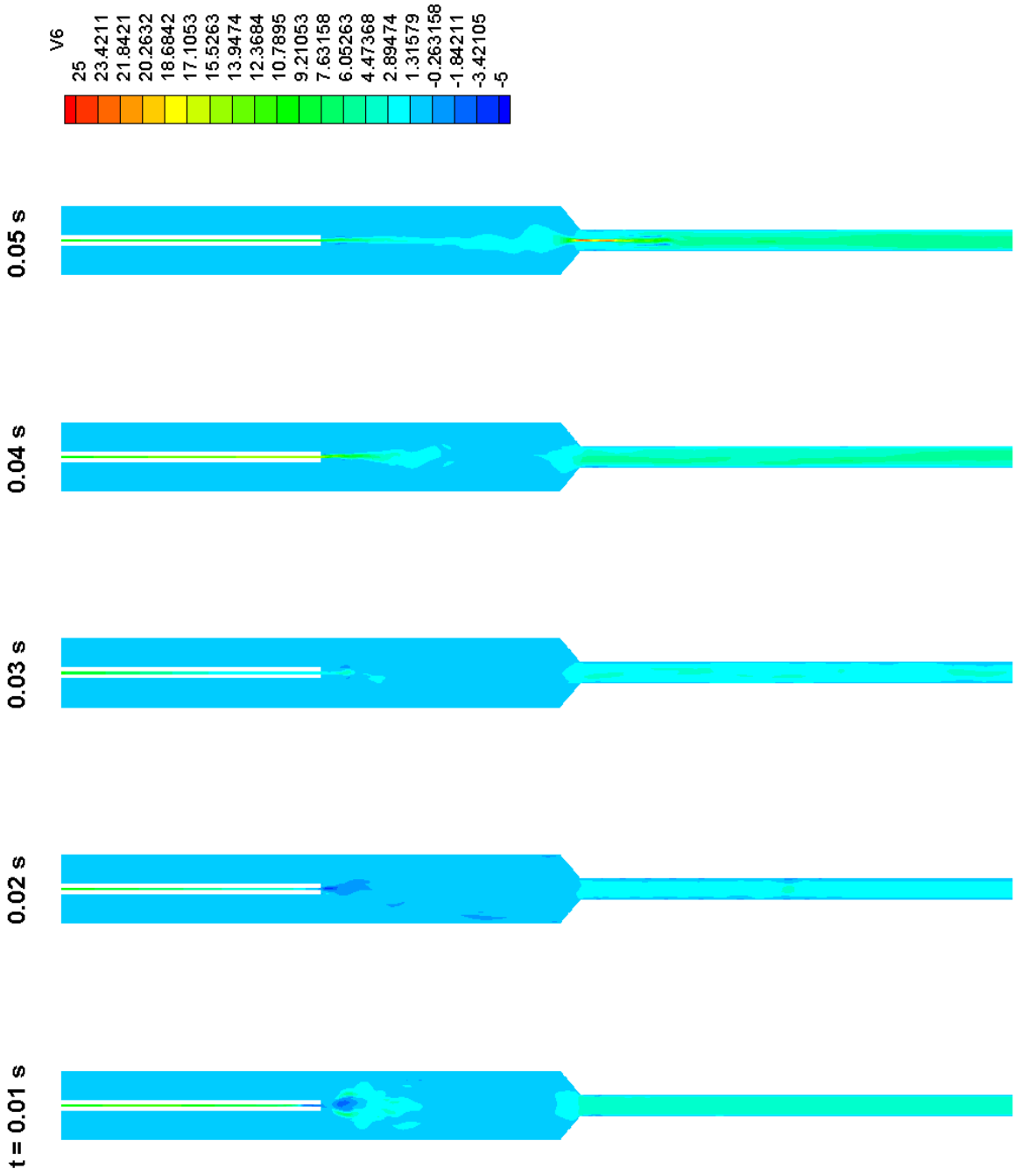

Figure 4.5: Axial velocity contours for Case 2, $V_{ref,un} = V_{ref}$

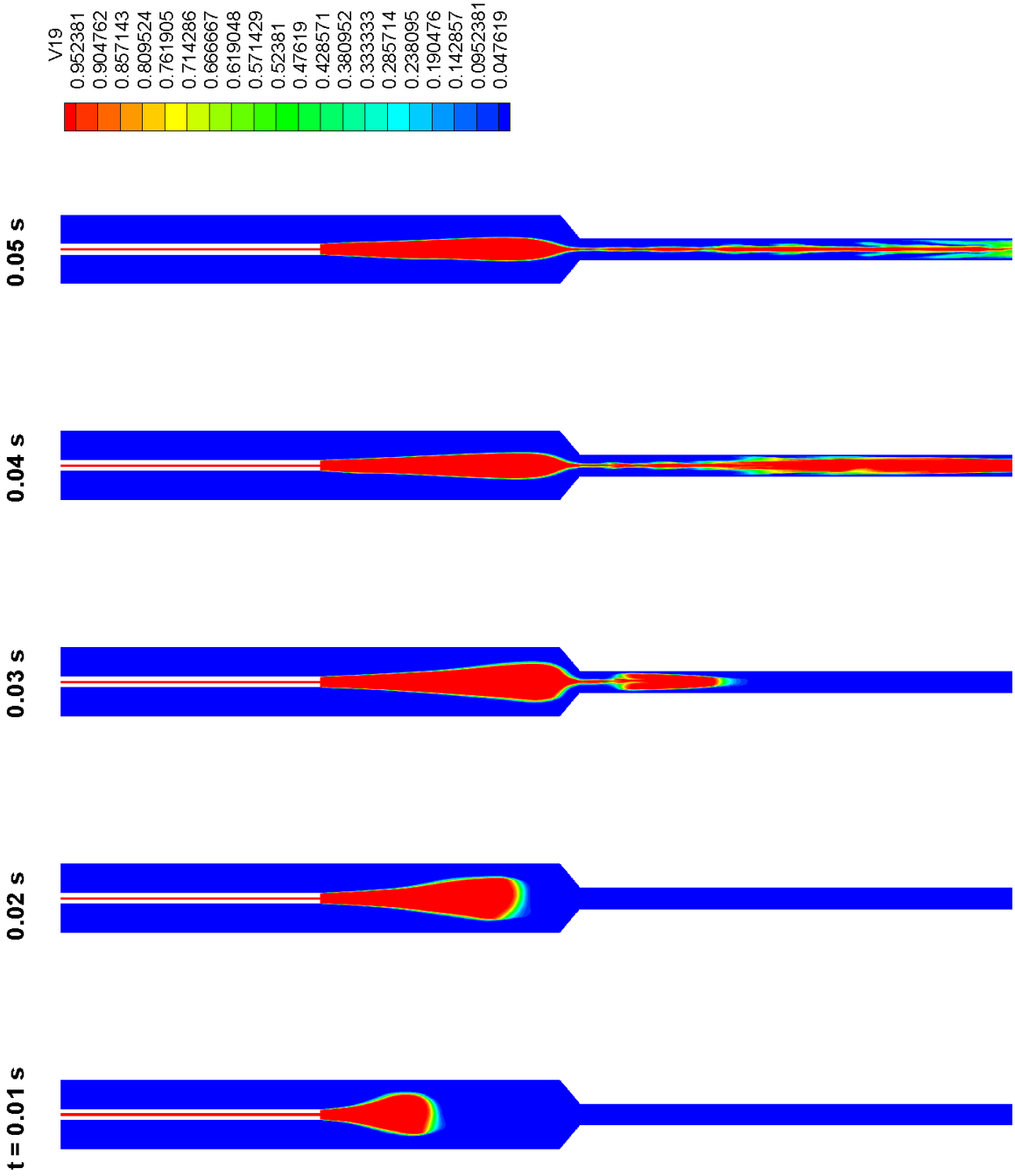

Figure 4.6: Gas-phase volume fraction contours for Case 3, $V_{ref} = V_{ref,un}$

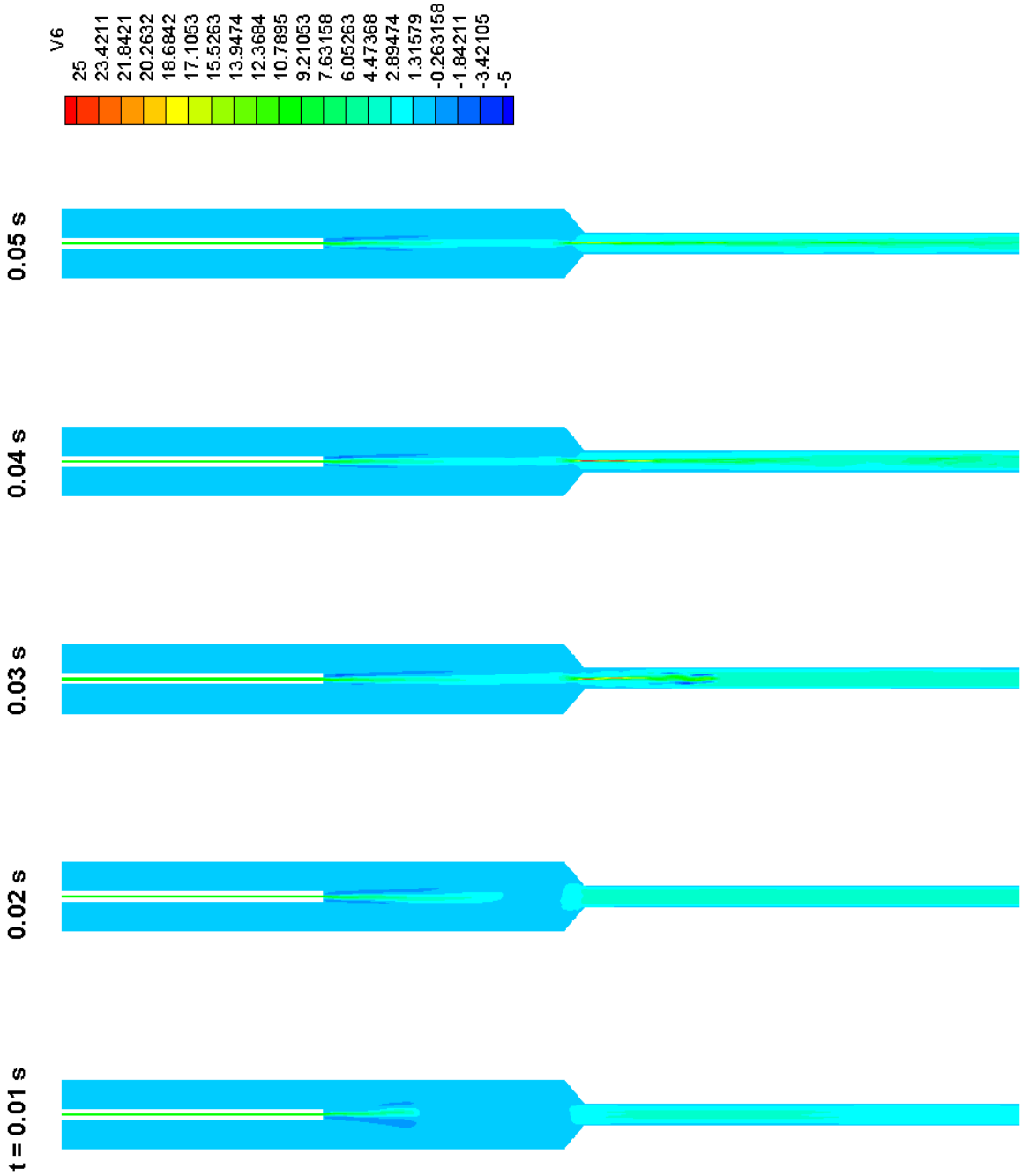

Figure 4.7: Axial velocity contours for Case 3, $V_{ref} = V_{ref,un}$

discharge passage is more like a core-annular flow, and overall, the flow appears much more steady in general than in Case 1. Axial velocity contours shown in Figure 4.7 illustrate that the vortex shedding phenomenon found in Cases 1 and 2 is significantly damped for Case 3, indicating that the use of the unsteady preconditioning reference velocity throughout is more dissipative for the velocity field.

In order to get a better understanding of the performance of these three cases, we analyze the gas mass conservation for all three cases. Figure 4.8 compares the gas mass ratios versus physical time iterations for Cases 1, 2 and 3. Each represents the ratio of the gas mass at any physical time iteration to that at the first physical time iteration. At each physical time step, a certain amount of gas enters the aerating tube from the inlet boundary and is recorded as the exact gas mass, $m_{g,e}$. Until the gas first exits the discharge passage orifice, the exact gas mass will increase linearly with increasing time, as the mass flow rate of the gas is held constant. Meanwhile, a numerical gas mass, $m_{g,n}$, is calculated by summing up the gas mass of each cell in the computational domain at each physical time step. It can be written as:

$$m_{g,n} = \int_V \rho Y_g dV \tag{4.1}$$

Thus, the numerical and exact gas mass ratios are defined respectively as:

$$\varphi_n = \frac{m_{g,n}}{(m_{g,n})_{\text{step 1}}}, \tag{4.2}$$

$$\varphi_e = \frac{m_{g,e}}{(m_{g,e})_{\text{step 1}}}. \tag{4.3}$$

In Figure 4.8, we find that the numerical gas mass ratio, φ_n, is very close to the exact gas mass ratio, φ_e, for Cases 1 and 3, but is very different from the exact gas mass ratio for Case 2. This indicates that the gas mass is not conserved well in Case 2. We also find that the numerical gas mass ratio increases until a certain time, t_{out}, which is about 7500 physical time steps, for Cases 1 and 3. After this time, the numerical gas mass ratio decreases. This implies that some gas flows out of the discharge passage

nozzle orifice. In Figure 4.8, we also find that $t_{\text{out},1} < t_{\text{out},3}$. This implies that the gas exits the discharge passage earlier in Case 1 than in Case 3.

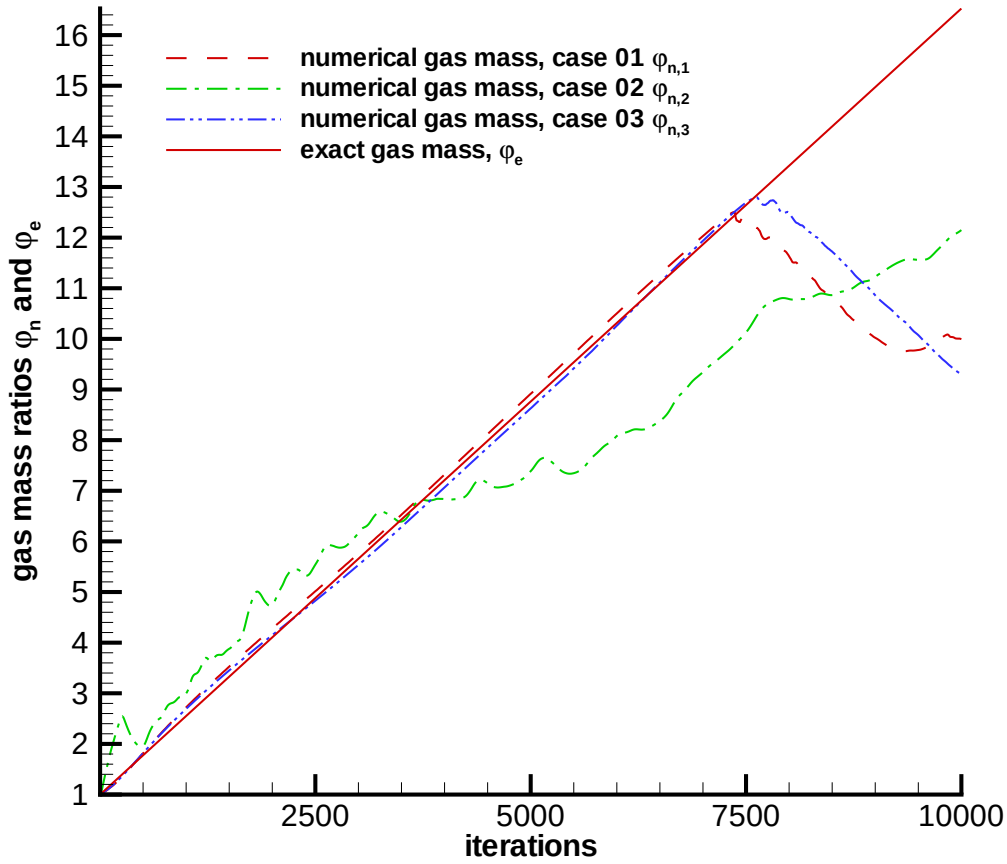

Figure 4.8: Comparison of gas mass ratio for Cases 1, 2 and 3

Furthermore, we make a error analysis of gas mass for all three cases. The relative error of gas mass is defined as:

$$\varepsilon = \left| \frac{\varphi_n - \varphi_e}{\varphi_n} \right|. \tag{4.4}$$

Figure 4.9 shows the relative errors of gas mass versus physical time steps for all three cases. In this figure, we find that the relative error, ε, is very small for Cases 1

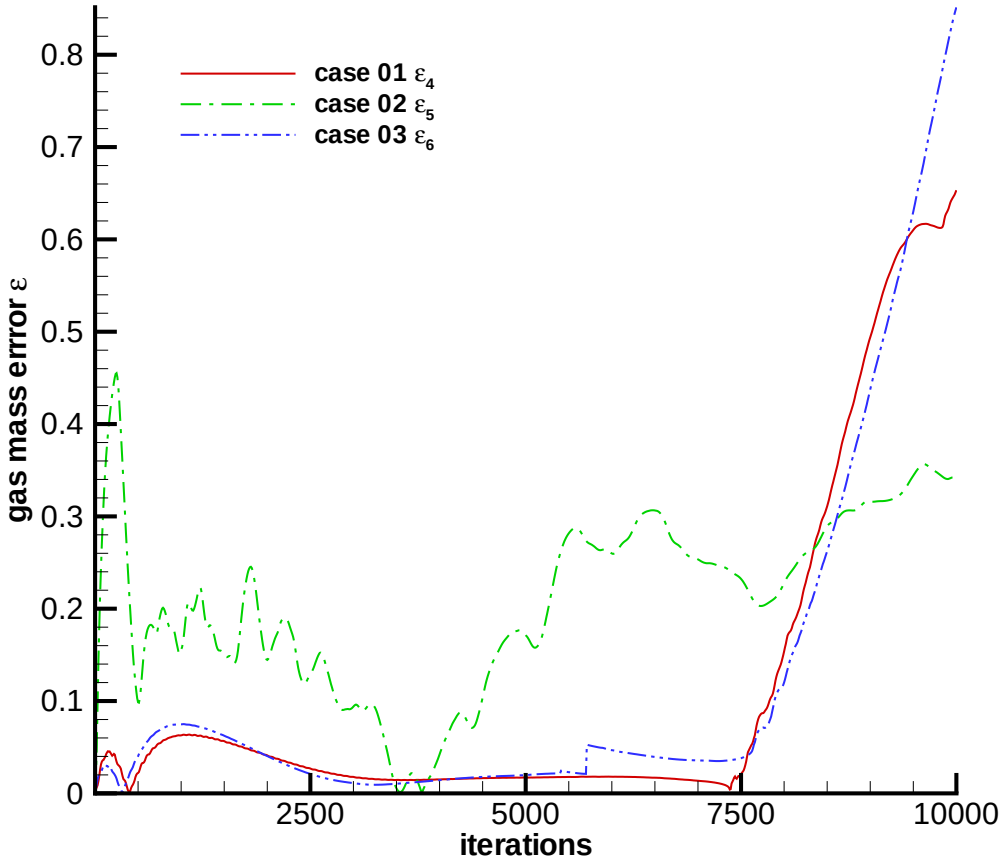

Figure 4.9: Comparison of gas mass ratio error for Cases 1, 2 and 3

and 3 before discharge occurs. The extreme value of ε_1 is about 6%, and that of ε_3 is about 7.5%. As for Case 2, ε_2 is very large, with a maximum value of about 45.5%. Again, this indicates that the gas mass is not conserved well in Case 2.

Figure 4.10 shows the mass flow rates of liquid ($m_{L,\text{in}}$ and $m_{L,\text{out}}$) at the inflow and outflow versus physical time iterations for Case 1. The mass flow rate of liquid at the inflow ($m_{L,\text{in}}$) for this case is fixed at a constant value of 6.51×10^{-3} kg/s, as per the experimental parameters. The mass flow rate of liquid at the outflow ($m_{L,\text{out}}$) oscillates with a large amplitude for the first 12000 iterations. This corresponds to the

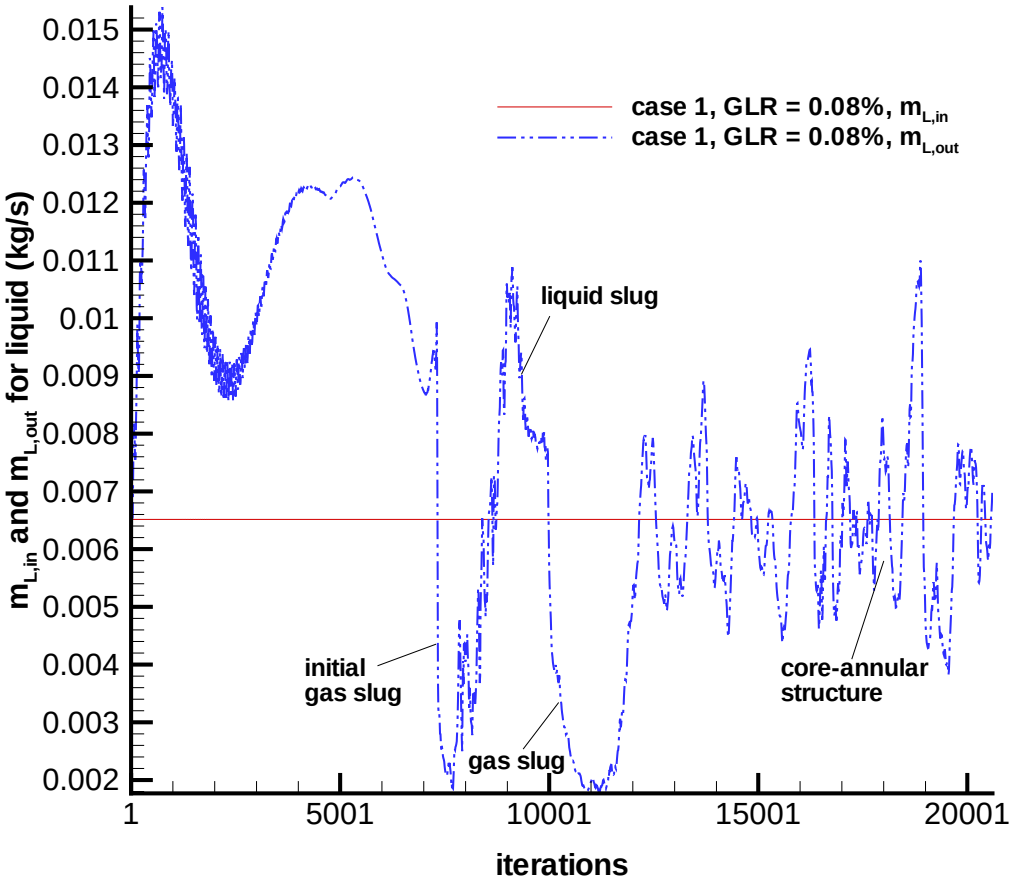

Figure 4.10: Mass flow rates of liquid at the inflow and outflow for Case 1

displacement of the liquid flow due to gas bubble growth. The average velocity of the liquid initially increases as the effective volume occupied by the liquid decreases. As time advances, $m_{L,\text{out}}$ eventually oscillates about $m_{L,\text{in}}$, implying that a statistically stationary state may have been reached. In Figure 4.10, the liquid mass flow rate at the outflow ($m_{L,\text{out}}$) has two extreme small values near 7500 iterations and near 11000 iterations, respectively. These bottom points indicate the passage of large slugs of gas, followed by slugs of liquid, through the exit of the discharge passage. After about 12000 iterations, the amplitude of the oscillation becomes smaller, and $m_{L,\text{out}}$

does not depart so far from $m_{L,\text{in}}$. This indicates that a core-annular flow pattern becomes dominant near the end of the discharge passage for long times.

4.1.2 Different Choices for the Surface Tension

The effects of surface tension are illustrated in Figure 4.11 and 4.12. Case 1 mentioned earlier is used as the baseline, with Cases 4 and 5 corresponding to 50% surface tension and no surface tension, respectively (see Table 4.2).

Table 4.2: Different choices for the surface tension

Case	Surface Tension
1	100%
4	50%
5	0%

Figure 4.11 shows gas-phase volume fraction contours for Case 4, where the surface tension calculated is multiplied by a factor of 0.5. Bubble generation for this case is very similar to that of Case 1, as is the structure of the gas-liquid mixing flow in the discharge passage.

Figure 4.12 shows gas-phase volume fraction contours for Case 5, where surface tension is neglected. Bubble generation is also very similar to that of Case 1, but in this case, the gas-liquid interface is less smooth and more irregular. One can note that the gas-liquid interface in the mixing chamber exhibits some wiggles for $t = 0.05$ seconds. These indicate that the interface is responding to the periodic shedding of vortices from the injector lip, whereas for higher values of the surface tension, the interface position is more resistant to these events.

Figure 4.13 compares gas mass ratios versus physical time iterations for Cases 1, 4 and 5. In Figure 4.13, we find that the numerical gas mass ratios, φ_n, are very close to the exact gas mass ratios, φ_e, for all three cases. This indicates that the gas

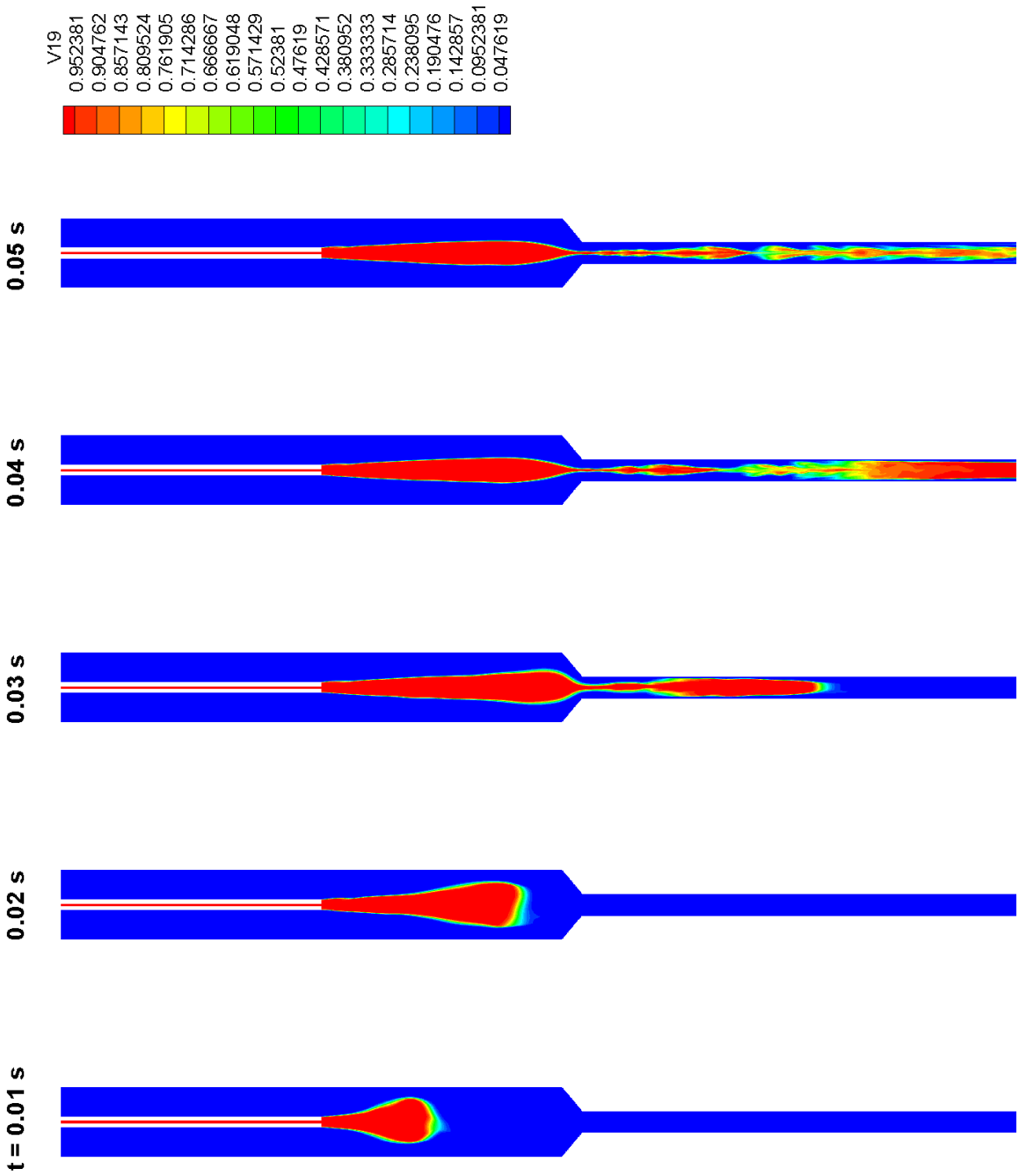

Figure 4.11: Gas-phase volume fraction contours for Case 4, 50% surface tension

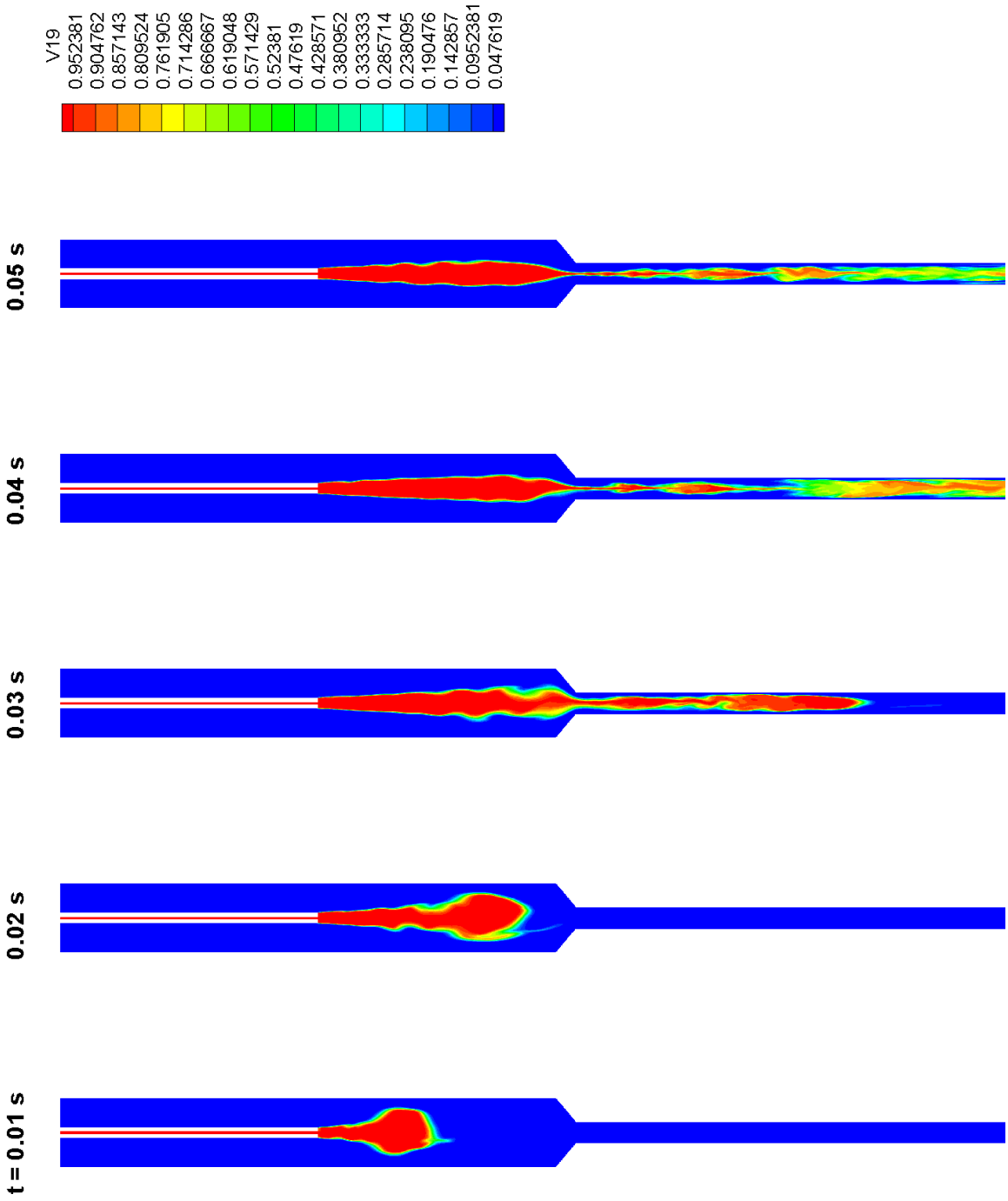

Figure 4.12: Gas-phase volume fraction contours for Case 5, no surface tension

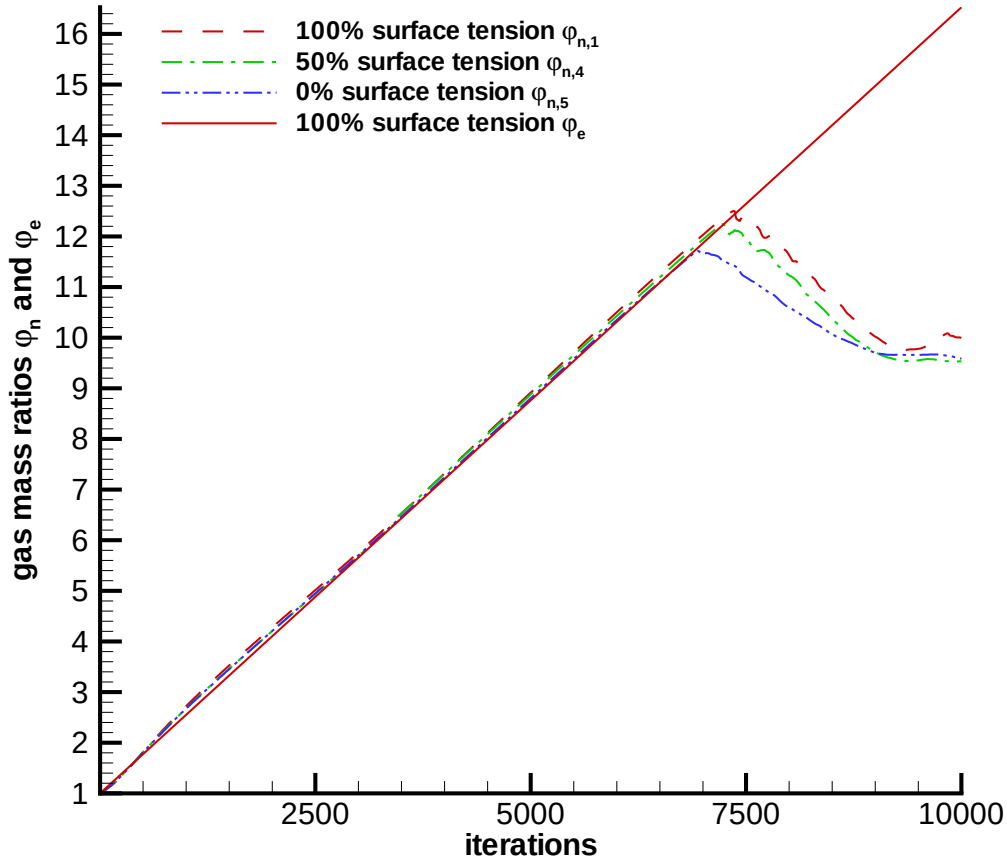

Figure 4.13: Comparison of gas mass ratio for Cases 1, 4 and 5

mass is conserved well in all three cases.

4.1.3 Bernoulli Inflow Boundary Condition for the Liquid Phase

The effects of different inflow boundary conditions for the liquid phase (see Table 4.3) are discussed in this section. Cases 1-5 correspond to a fixed volume flow rate for the incoming liquid, while in Case 6, we consider a Bernoulli inflow boundary condition for the liquid phase, which is defined in Section 3.3. For this case, the number of physical time iterations was about 30000.

Table 4.3: Different choices for the inflow boundary condition for the liquid phase

Case	Inflow Boundary Condition for the Liquid Phase
1-5	fix u, v, w, T, Y_g, etc., extrapolate p.
6	fix p_0, v, w, T, Y_g, etc., extrapolate u.

Figure 4.14 shows gas-phase volume fraction contours for Case 6, where the Bernoulli inflow boundary condition is used for the liquid phase. Twelve contours in this figure reveal the generation and the evolution of the bubbles in the mixing chamber and the discharge passage for Case 6. In Case 6, the dynamics of bubble formation and growth is somewhat different from that of Case 1. In this case, the bubble breaks up once in the mixing chamber (0.06 and 0.07 seconds) before shrinking to a thin line upon entering the converging section. The start of another break-up event is seen in the contours corresponding to 0.12 seconds. The structure of the gas-liquid mixing flow in the discharge passage is more characteristic of a slugging flow, though core-annular features do appear at different time levels.

Comparing Figure 4.2 and 4.14 or Figure 4.3 and 4.15, we find that the velocity of the gas-liquid mixing flow is slower in Case 6 than in Case 1. At about 0.04 seconds, the gas-liquid mixing flow ejects the discharge nozzle orifice in Case 1, but it just enters the discharge nozzle in Case 6. Another finding is that the size of the bubble in Case 6 is larger than that in Case 1. In Case 6, we also find that as time progresses, the bubble shape continues to change in the mixing chamber, whereas in Case 1, the bubble shape reaches a steady state in this region. These trends are related to the fact that, with the Bernoulli boundary condition, the mass flow rate is not constant and in fact, generally drops with gas injection.

Figure 4.16 shows gas mass ratio versus time iterations for Case 6. In Figure 4.16, we find that the numerical gas mass ratio, φ_n, is very close to the exact gas mass

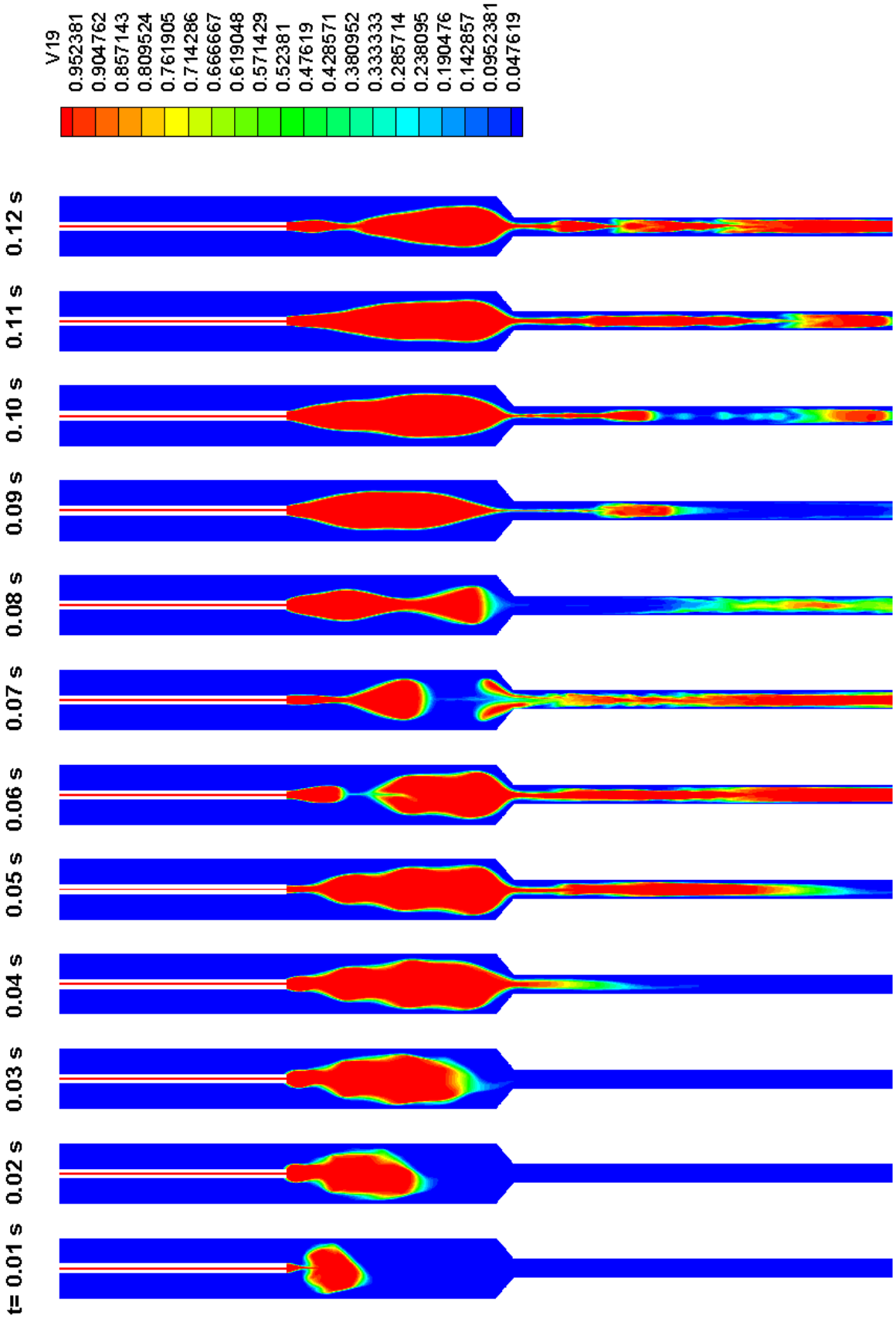

Figure 4.14: Gas-phase volume fraction contours with Bernoulli inflow B.C.

Figure 4.15: Axial velocity contours with Bernoulli inflow B.C.

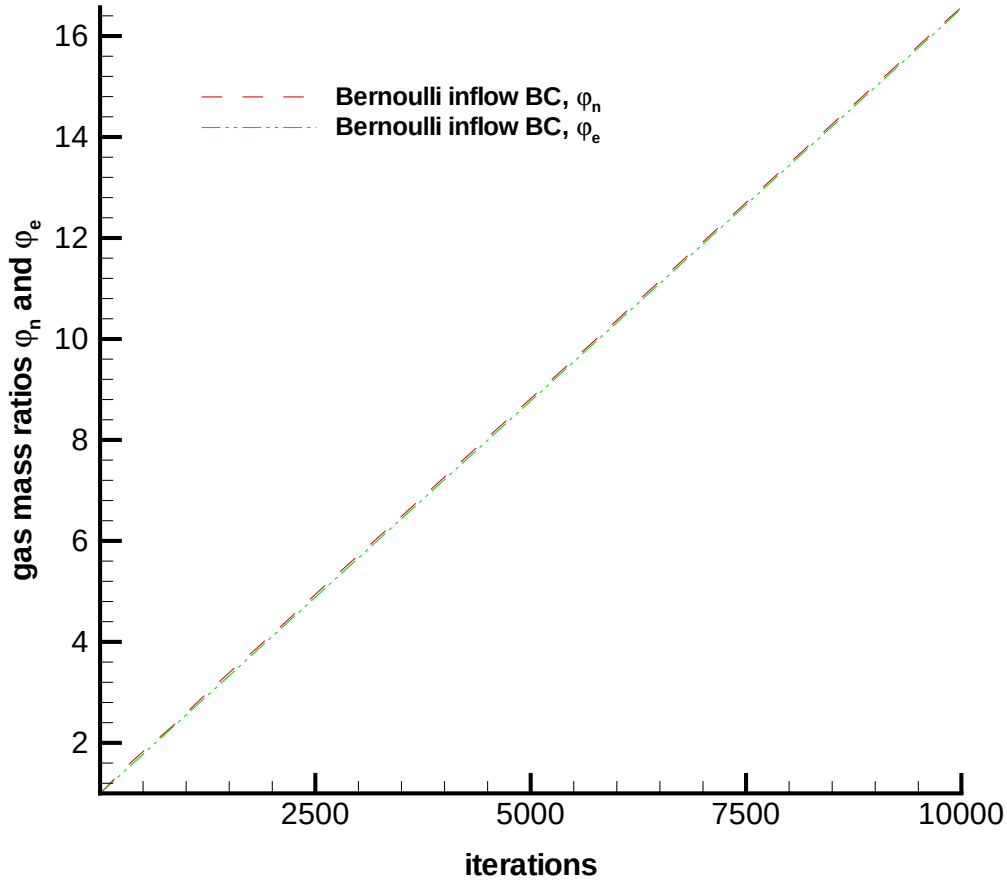

Figure 4.16: Gas mass ratio versus iterations with Bernoulli inflow B.C.

ratio, φ_e. This indicates that the gas mass is conserved very well in this case. We also find that the numerical gas mass ratio increases monotonically for 10000 physical time steps, as opposed to about 7500 iterations for Case 1. This again confirms that the gas-liquid mixing flow has a slower average velocity than that in Case 1.

Figure 4.17 shows the relative error of gas mass versus physical time steps for Case 6. In this figure, we find that the relative error, ε, is smaller than that of Case 1. Recall that the extreme value of ε_1 is about 6%. However, the extreme value of ε_6 is about 3.4%. This indicates that the use of Bernoulli inflow boundary condition

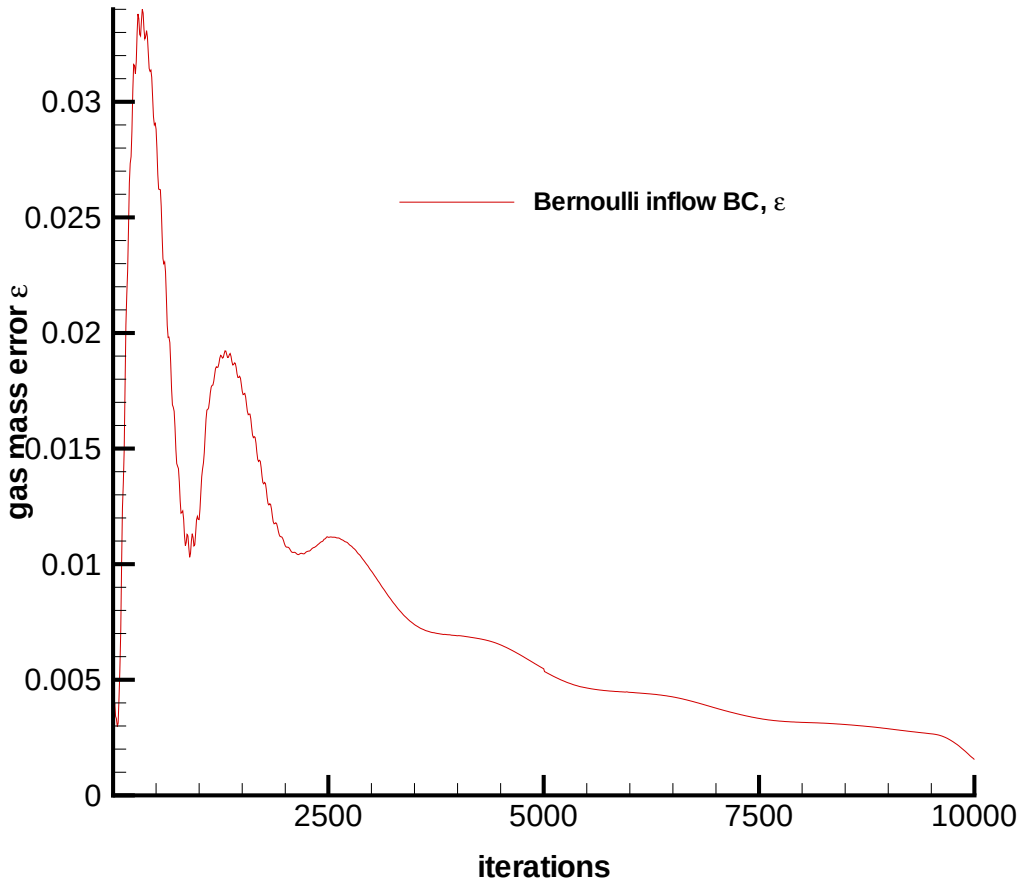

Figure 4.17: Gas mass ratio error versus iterations with Bernoulli inflow B.C.

leads to slightly better gas conservation.

Figure 4.18 shows the mass flow rates of liquid ($m_{L,\text{in}}$ and $m_{L,\text{out}}$) at the inflow and outflow versus physical time iterations for Case 6. The mass flow rate of liquid at the inflow ($m_{L,\text{in}}$) for this case oscillates and does not converge. This is unlike the behavior of Case 1, but is the expected result, since total pressure, rather than velocity is specified. As in Case 6, the mass flow rate of liquid at the outflow ($m_{L,\text{out}}$) also oscillates, but the dynamics are quite different. In the $m_{L,\text{out}}$ curve, we find that one extreme small value occurs near 12000 iterations, and one peak value occurs

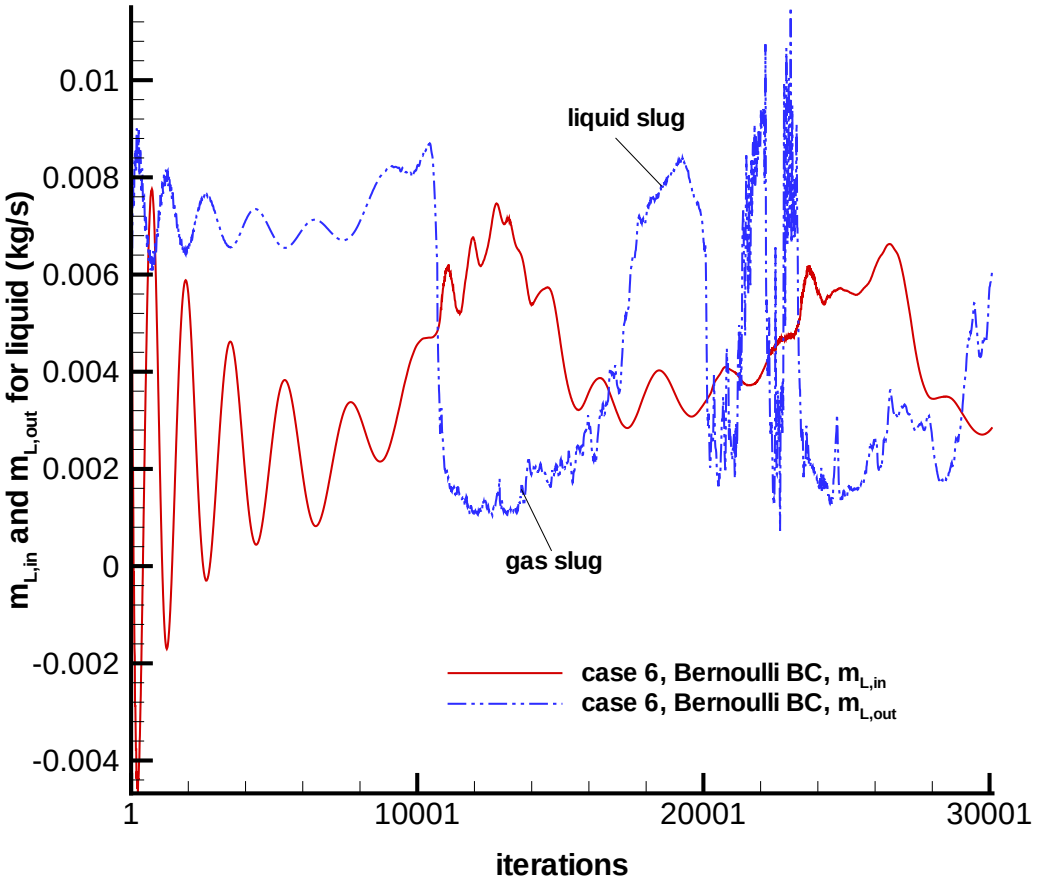

Figure 4.18: Mass flow rates of liquid at the inflow and outflow with Bernoulli inflow B.C.

near 19000 iterations. The former point indicates that a slug of gas exits through the outflow boundary. The latter one indicates that a slug of liquid exits from the boundary. The $m_{L,\text{out}}$ curve has other such points. This indicates that a slug flow pattern is predominant when Bernoulli inflow boundary conditions are used. It is not clear whether the flow can be regarded as statistically stationary at this point; if so, it seems that the system has relaxed to an average mass flow of about 4.5×10^{-3} kg/s, about 30% less than the experimental value of 6.51×10^{-3} kg/s.

4.2 $GLR = 2.45\%$ Simulations

Results for a higher gas-to-liquid mass ratio of 2.45% are presented in this section. The nominal inflow pressures of gas and liquid are 137126.0 Pa and 101325.0 Pa, respectively. The nominal temperature is 300 K. The nominal inflow velocity of liquid is 0.586 m/s. The mass flow rate per unit area for gas ($(\rho u)_g$) is 351.238 kg/(m^2·s).

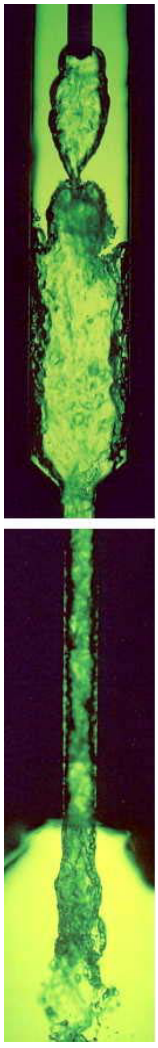

Figure 4.19: Experimental photographs for the structure of internal two-phase flow inside an aerated-liquid injector, $Q_L = 0.38$ l/min, $GLR = 2.45\%$

Figure 4.19 illustrates the experimental photographs of the structure of the internal two-phase flows inside the aerated-liquid injectors with $Q_L = 0.38$ l/min, $GLR =$

2.45%. As the aeration level is raised to a GLR of 2.45%, shown in Figure 4.19, Lin and coworkers [1] find that the structure of the two-phase flow in this case is very different from that for a GLR of 0.08%. They find that no individual bubbles are formed from the aerating tube orifice. Instead, a separated region, extending over a significant portion of the mixing chamber, is filled with the aerating gas. The liquid, consequently, is squeezed into a thin film attached to the walls of the mixing chamber. The resulting two-phase flow at the exit of the final discharge passage is a turbulent co-annular flow, with the aerating gas flowing in the core region. As can be seen in Figure 4.19, the thickness of the liquid film inside the discharge passage is not constant. The wavy interface indicates an increase in relative velocity between the liquid and aerating gas.

Figure 4.20 shows the volume fraction contours of gas phase for Case 7, where a GLR of 2.45% is used in the simulations. These contours were extracted every 500 physical time iterations, or every 2.5×10^{-3} seconds. A smaller time step of 1.25×10^{-6} seconds was used in these calculations, due to the need to resolve a higher speed gas flow.

Ten contours in this figure reveal the generation and the evolution of the bubbles in the mixing chamber and the discharge passage for Case 7. Bubble generation is very similar to the experiments. In this case, distinct bubbles are not found in the mixing chamber. Instead, as in the experiment, a separated region, extending over a large portion of the mixing chamber, is filled with the aerating gas, squeezing the liquid into a thin film attached to the walls of the mixing chamber and the discharge passage. A core-annular structure thus results, with the aerating gas flowing in the core region.

Figure 4.21 presents axial velocity contours for Case 7 with a GLR of 2.45%. The flow is much less organized and is indicative of a highly turbulent flow, even if

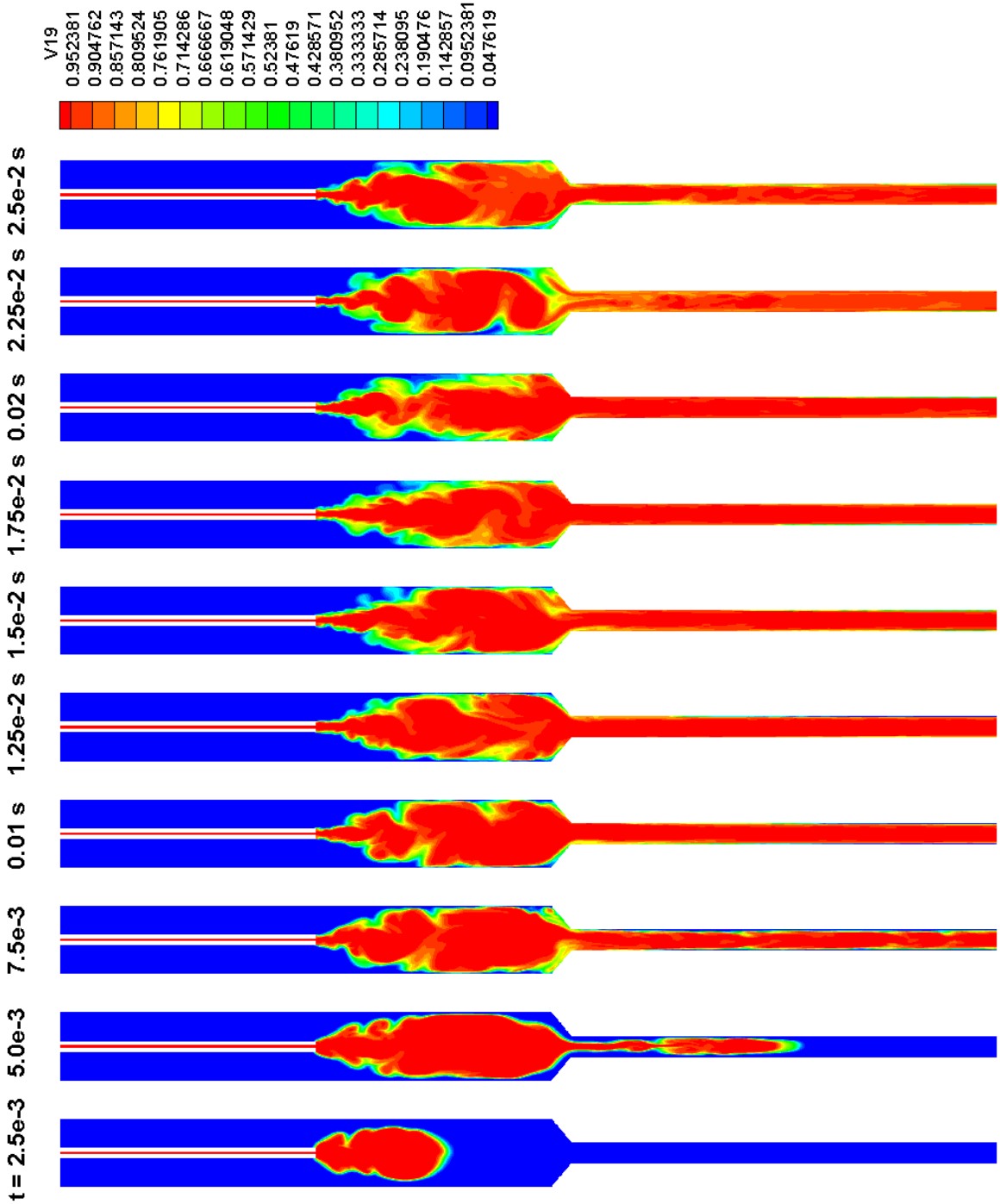

Figure 4.20: Volume fraction contours of gas phase with $GLR = 2.45\%$

Figure 4.21: Axial velocity contours with $GLR = 2.45\%$

simplified to two dimensions. The maximum velocity is achieved at the injector tube exit, but very high-speed gas is also found within the tube and at the entrance to the discharge passage. Mach number contours (not shown) indicate that the discharge passage flow is greater than Mach 0.6 on the average, with localized pockets of near sonic flow occurring at random intervals. This relatively high Mach number is due both to the high speed of the gas flow and to the low sound speed characteristic of a two-phase mixture.

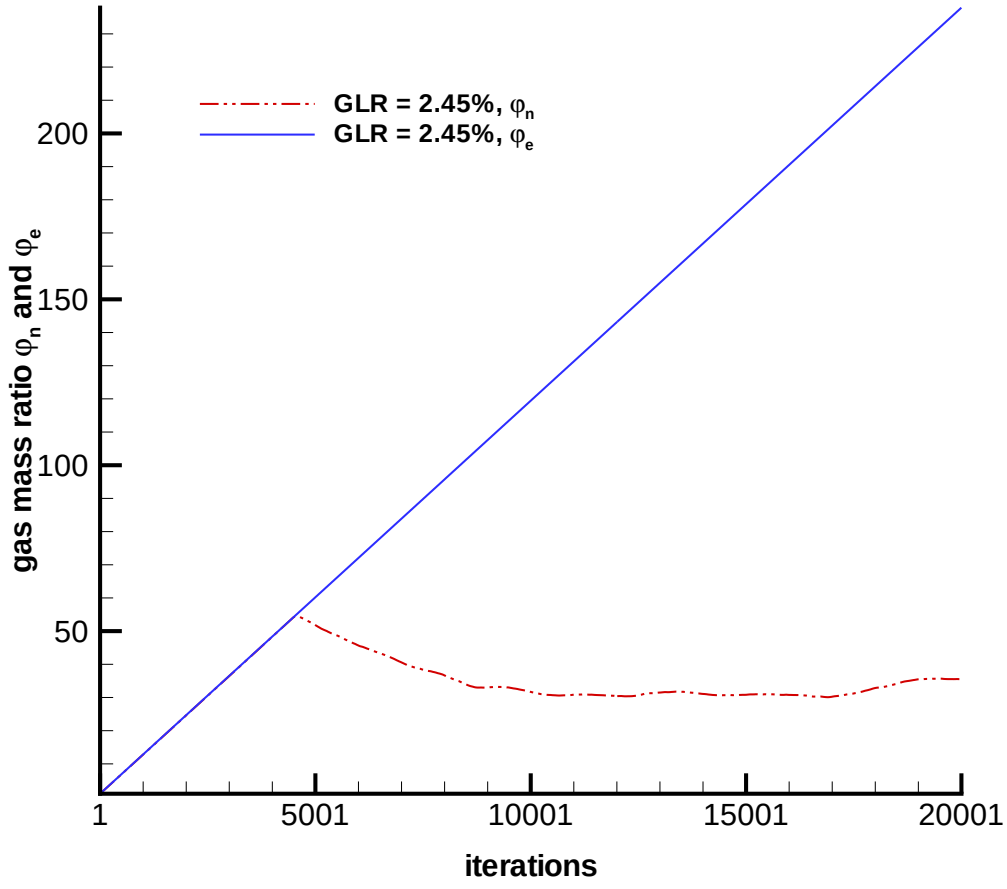

Figure 4.22: Gas mass ratio versus iterations with $GLR = 2.45\%$

Figure 4.22 shows gas mass ratio versus physical time iterations for Case 7. In

Figure 4.22, we find that the numerical gas mass ratio, φ_n, matches almost perfectly with the exact gas mass ratio, φ_e before a certain time, t_{out}, which is about at 4600 physical time steps. This indicates that the gas mass is conserved very well in this case. After t_{out}, the numerical gas mass ratio decreases, as gas begins to exit the discharge passage.

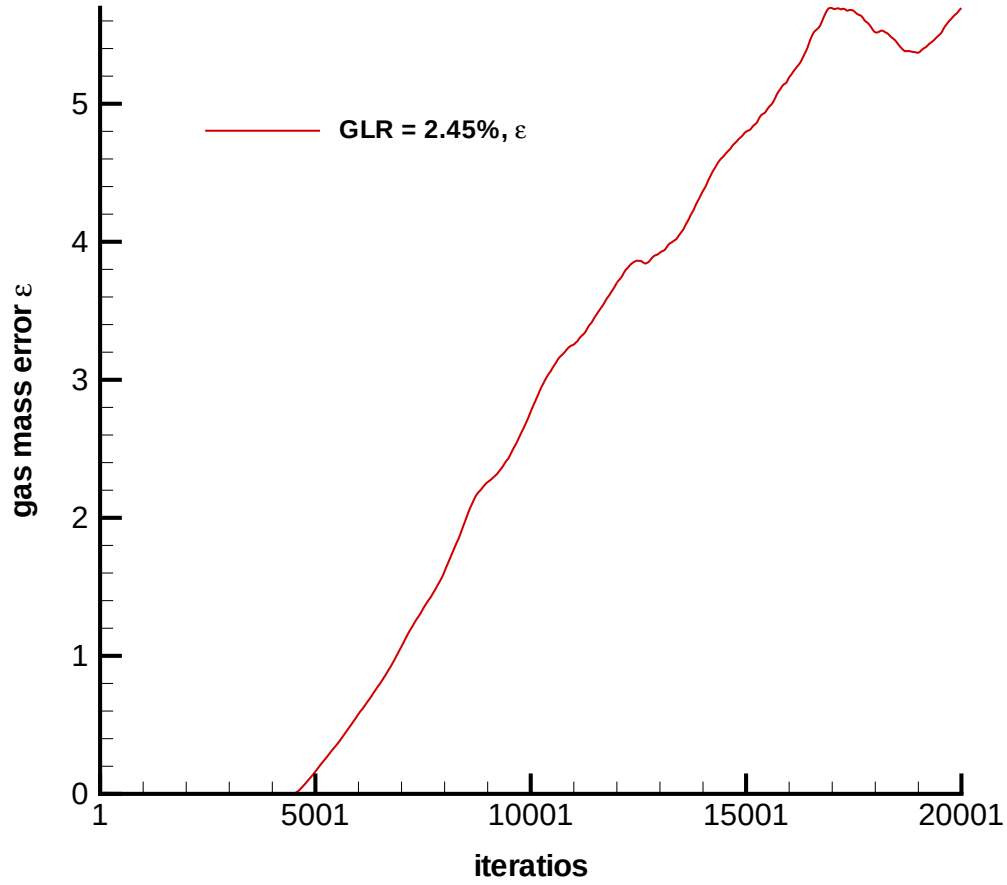

Figure 4.23: Gas mass ratio error versus iterations with $GLR = 2.45\%$

Figure 4.23 shows the relative error of gas mass versus physical time steps for Case 7. In this figure, we find that the relative error, ε, is nearly zero before t_{out} for Case 7. This also confirms that the gas mass is conserved very well in this case. If

we have a close look at the gas mass error between 0 to 4600 physical time iterations, we find that the extreme value of ϵ is about 0.7%, a value much smaller than that of $GLR = 0.08\%$ cases. This can be attributed to the lower time step used in these calculations.

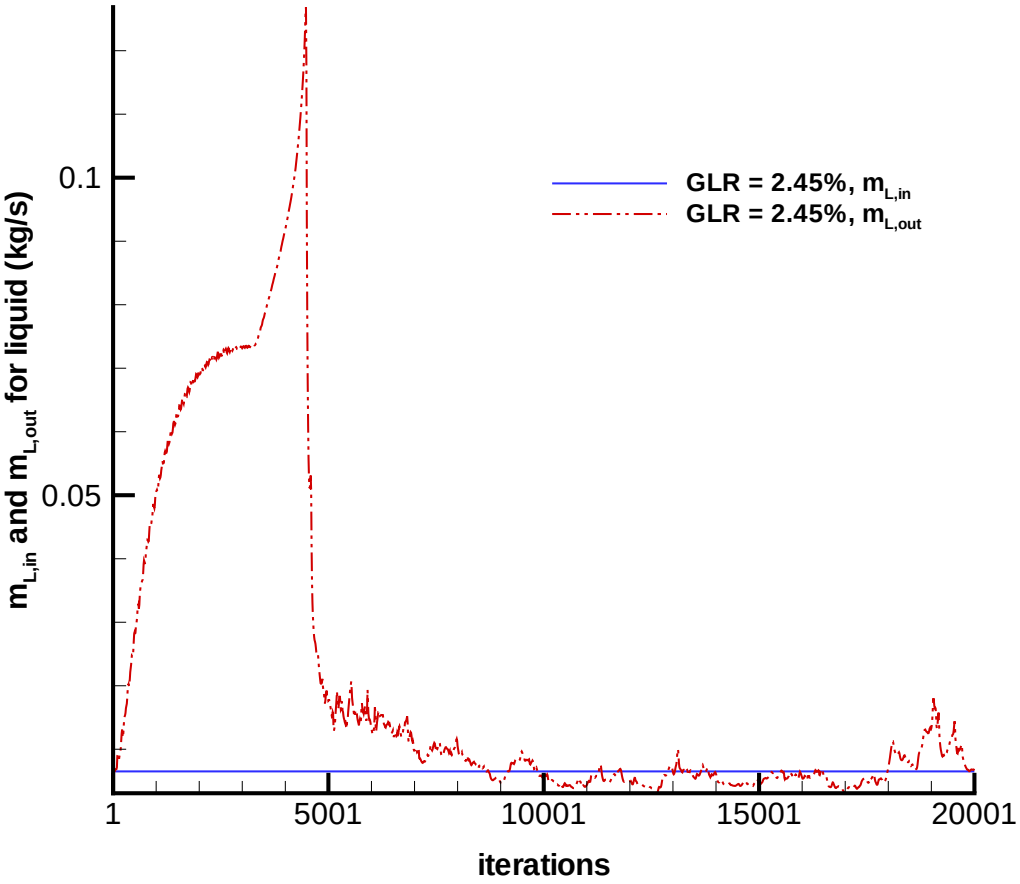

Figure 4.24: Mass flow rates of liquid at the inflow and outflow with $GLR = 2.45\%$

Figure 4.24 shows the mass flow rates of liquid at the inflow and outflow ($m_{L,\text{in}}$ and $m_{L,\text{out}}$) versus physical time iterations for Case 7. The mass flow rate of liquid at the inflow ($m_{L,\text{in}}$) is fixed at the experimental value of 6.5×10^{-3} kg/s. The mass flow rates of the liquid at the outflow ($m_{L,\text{out}}$) for this case increases monotonically before

t_{out}, which is at about 4600 physical time iterations. $m_{L,\text{out}}$ reaches its peak value at t_{out}. This implies that the liquid flow is accelerated significantly due to the blockage caused by the gas injection. After t_{out}, $m_{L,\text{out}}$ oscillates with a small amplitude about $m_{L,\text{in}}$, indicating that a statistically steady state, characterized by a core-annular flow pattern, may have been reached.

5 Conclusions

A time-derivative preconditioning method using the Low-Diffusion Flux-Splitting Scheme (LDFSS) has been extended to a mixture model of two-phase flow and applied to simulate the internal two-phase flow within aerated-liquid injectors.

The mixture model of two-phase flow is tested and evaluated for two different gas-to-liquid (GLR) mass ratios: 0.08% and 2.45%. Seven cases are simulated in this study. In the $GLR = 0.08\%$ simulations, different choices for the reference velocities are tested as Cases 1, 2 and 3; different choices for surface tension are tested as Cases 4 and 5; and the use of a Bernoulli inflow boundary conditions for the liquid phase is tested as Case 6.

The results of Cases 1, 2 and 3 indicate that if we calculate V_{ref} and $V_{ref,un}$ separately (Case 1), the performance on gas mass conservation is the best, though the bubble does not break up in the mixing chamber as in the experiment. Reasons may include geometry differences, three-dimensional effects, and turbulent effects. The structure of the two-phase flow in the discharge passage is a combination of slugging flow and core-annular flow. If we implement steady preconditioning for the whole system (Case 2), the bubble does separate in the mixing chamber, but gas mass is not conserved. The results of Cases 1, 4 and 5 indicate that inclusion of surface tension promotes more rounded and smoother gas-liquid interfaces that are more resistant to hydrodynamic effects. The results of Case 6 indicate that the use of a Bernoulli inflow boundary condition for the liquid phase makes the bubble break up in the mixing chamber, the mass flow rate of the liquid is lower, on the average, than the experimental value.

In $GLR = 2.45\%$ simulation, only one case is tested. The results of Case 7 indicate that the computed flow structure is very similar to the experiment. In this case, no individual bubbles are formed from the aerating tube orifice. Instead, a

separated region, extending over a large portion of the mixing chamber, is filled with the aerating gas. The liquid, consequently, is squeezed into a thin film attached to the walls of the mixing chamber. The resulting two-phase flow in the discharge passage is a core-annular flow, with the aerating gas flowing in the core region.

6 Future Work

There are several areas of extension for the current work:

1. Simulation of additional cases at different liquid volume flow rates and different gas-to-liquid mass ratios,

2. Three-dimensional simulations of the aerated-liquid injector flowfields,

3. Inclusion of a turbulence model,

4. coupling the code with a droplet-tracking algorithm to simulate the resulting spray development.

The first area is a fairly simple extension. In order to compare with the experimental results, more simulations should be made under different volumetric flow rates (Q_L) with different gas-to-liquid mass ratios (GLR).

Since in the current study, we only consider 2-D injectors, the effects of the real 3-D geometry are ignored. This alone could be a major reason for the observed discrepancies in company with experiment. Three-dimensional simulations will be much more expensive to run and will require a complex grid topology to render a circular aerating gas injector within a rectangular nozzle.

We only consider laminar flows in the current work. The actual flow is probably turbulent, particularly at the higher GLR ratios. We will consider both Reynolds-Averaged turbulence modeling strategies as well as hybrid Reynolds-Averaged / Large-Eddy Simulations in future work.

We only investigate the two-phase flow inside the aerated-liquid injector in the current work. In order to understand the mechanisms that may lead to formation of smaller droplets, we should also consider the corresponding spray area for the aerated-liquid injector.

References

[1] Lin, K. C., Kennedy, P., J., and Jackson, T. A., "Structures of Internal Flow and the Corresponding Spray for Aerated-Liquid Injectors," AIAA Paper 2001-3569, 2001. 1, 34, 35, 65

[2] Turkel, E., "Preconditioned Methods for Solving the Incompressible and Low Speed Compressible Equations," *Journal of Computational Physics*, Vol. 72, 1987, pp. 277–298. 1, 22, 23

[3] Choi, Y. H. and Merkle, C. L., "The Application of Preconditioning in Viscous Flows," *Journal of Computational Physics*, Vol. 105, 1993, pp. 207–223. 1, 22, 23

[4] Weiss, J. M. and Smith, W. A., "Preconditioning Applied to Variable and Constant Density Time-Accurate Flows on Unstructured Meshes," AIAA Paper 1994-2209, June 1994. 1, 22, 23

[5] Turkel, E., "Preconditioning Techniques in Computational Fluid Dynamics," *Annual Review of Fluid Mechanics*, Vol. 31, 1999, pp. 385–416. 1, 22, 23

[6] Venkateswaran, S. and Merkle, C. L., "Dual Time Stepping and Preconditioning for Unsteady Computations," AIAA Paper 1995-0078, January 1995. 1, 22, 23, 30

[7] Venkateswaran, S. and Merkle, C. L., "Analysis of Preconditioning Methods for the Euler and Navier-Stokes Equations," Lecture notes prepared for the 30th computational fluid dynamics lecture series program of the von karman institute (vki) for fluid dynamics, rhode-saint genese, belgium, march 15-17,1999-03, 1999. 1, 22

[8] Venkateswaran, S. and Merkle, C. L., "Efficiency and Accuracy Issues in Contemporary CFD Algorithms," AIAA Paper 2000-2251, June 2000. 1, 22, 23

[9] Edwards, J. R., "A Low-Diffusion Flux-Splitting Scheme for Navier-Stokes Calculations," *Computers and Fluids*, Vol. 26, No. 6, 1997, pp. 635–659. 1, 26, 81

[10] Edwards, J. R., "Towards Unified CFD Simulation of Real Fluid Flows," AIAA Paper 2001-2524, June 2001. 1, 22, 26

[11] Drew, D. A. and Lahey, R. T., "Application of General Constitutive principles of the Derivation of Multidimensional Two-Phase Flow Equations," *International Journal of Multiphase Flow*, Vol. 5, 1979, pp. 243–264.

[12] Tannehill, J. C., Anderson, D. A., and Pletcher, R. H., *Computational Fluid Mechanics and Heat Transfer*, Taylor and Francis, Washington DC, 2nd ed., 1997. 14

[13] McBride, B. J., Gordon, S., and Reno, M. A., "Coefficients for Calculating Thermodynamic and Transport Properties of Individual Species," NASA TM-4513, October 1993. 15

[14] Wilke, C. R., "A Viscosity Equation for Gas Mixtures," *Chemical Physics*, Vol. 18, No. 4, April 1950, pp. 517–519. 16

[15] Saurel, R., Cocchi, J. P., and Butler, P. B., "Numerical Study of Cavitation in the Wake of a Hypervelocity Underwater Projectile," *Journal of Propulsion and Power*, Vol. 15, No. 4, July-August 1999, pp. 513–522. 17

[16] Oldenbourg, R., *Properties of Water and Stream in SI-Units*, Springer-Verlag, Berlin, 1989. 17

[17] Lide, D. R. and Kehiaian, H. V., *CRC Handbook of Thermophysical and Thermochemical Data*, CRC Press, Inc., 1994. 18

[18] Brackbill, J. U., Kothe, D. B., and Zemach, C., "A Continuum Method for Modeling Surface Tension," *Journal of Computational Physics*, Vol. 100, 1992, pp. 335–354. 19

[19] Chorin, A. J., "A Numerical Method for Solving Incompressible Viscous Flow Problems," *Journal of Computational Physics*, Vol. 2, 1967, pp. 12–26. 24

[20] Liou, M.-S. and Edwards, J. R., "Numerical Speed of Sound and its Application to Schemes for All Speeds," AIAA Paper 1999-3268-CP, June 1999. 26

[21] Liou, M.-S. and Edwards, J. R., "AUSM Schemes and Extensions for Low Mach and Multiphase Flows," Lecture notes prepared for the 30th computational fluid dynamics lecture series program of the von karman institute (vki) for fluid dynamics, rhode-saint genese, belgium, march 15-17,1999-03, 1999. 26

[22] Liou, M.-S. and Steffen, C. J., "A New Flux Splitting Scheme," *Journal of Computational Physics*, Vol. 107, 1993, pp. 23–39. 26, 29

[23] Liou, M.-S., "Ten Years in the Making—AUSM-family," AIAA Paper 2001-2521, June 2001. 26

[24] Edwards, J. R., "A Low-Diffusion Flux-Splitting Scheme for Navier-Stokes Calculations," AIAA Paper 1995-1703-CP, June 1997.

[25] Edwards, J. R. and Liou, M.-S., "Low-Diffusion Flux-Splitting Methods for Flows at All Speeds," *AIAA Journal*, Vol. 36, No. 9, 1998, pp. 1610–1617. 26

[26] Liou, M.-S., "Progress Towards an Improved CFD Method: AUSM+," AIAA Paper 1995-1701, June 1995. 27, 29

[27] Fan, T. C., Tian, M., Edwards, R., J., Hassan, H. A., and Baurle, R. A., "Validation of a Hybrid Reynolds-Averaged/Large-Eddy Simulation Method for Simulating Cavity Flameholder Configurations," AIAA Paper 2001-2929, June 2001. 29

[28] Fan, T. C., Xiao, X., Edwards, J. R., Hassan, H. A., and Baurle, R. A., "Hybrid LES/RANS Simulation of a Shock Wave / Boundary Layer Interaction," AIAA Paper 2002-0431, January 2002. 29

[29] van Albada, G. D., van Leer, B., and Roberts, Jr, W. W., "A Comparative Study of Computational Methods in Cosmic Gas Dynamics," *Astronomy & Astrophysics*, Vol. 108, 1982, pp. 76–84. 30

[30] Hirsch, C., *Computational Methods for Inviscid and Viscous Flows*, Vol. 2 of *Numerical Computation of Internal and External Flows*, John Wiley & Sons Ltd., 1984. 30

[31] Edwards, J. R., "Development of an Upwind Relaxation Multigrid Method for Computing Three-dimensional, Viscous Internal Flows," *Journal of Propulsion and Power*, Vol. 12, No. 1, 1996, pp. 145–154. 30

[32] Edwards, J. R., "Advanced Implicit Methods for Finite-Rate Hydrogen-Air Combustion Calculations," AIAA Paper 1996-3129, July 1996. 30

[33] Roy, C. J., *A computational Study of Turbulent Reacting Flowfields for Scramjet Applications*, Ph.D. thesis, North Carolina State University, 1998. 31

[34] Snir, M., Otto, S., Lederman, S. H., Walker, D., and Dongarra, J., *MPI: The Complete reference*, The MIT Press, 1996. 36

[35] Aoyama, Y. and Nakano, J., *RS/6000 SP: Practical MPI Programming*, IBM Corporation, 1999. 36

Appendices

A Real Fluid Sound Speed

In order to determine the speed of sound in the mixture of gas and liquid used for the aerated-liquid injector simulation, an eigenvalue analysis is employed with the notion of a generalized equation of state.

$$\rho = \rho\left(p, T\right), \qquad h = h\left(p, T\right) \tag{a-1}$$

A one-dimensional Euler system of fluid equations is used to determine the eigenvalues for simplicity,

$$\frac{\partial \mathbf{U}}{\partial t} + \frac{\partial \mathbf{E}}{\partial x} = 0 \tag{a-2}$$

where the vector of conservative variables $\mathbf{U}$, the flux vector $\mathbf{E}$, and the vector of primitive variable set $\mathbf{V}$ are defined here as

$$\mathbf{U} = \begin{bmatrix} \rho \\ \rho u \\ \rho H - p \end{bmatrix}, \quad \mathbf{E} = \begin{bmatrix} \rho u \\ \rho u^2 + p \\ \rho H u \end{bmatrix}, \quad \mathbf{V} = \begin{bmatrix} p \\ u \\ T \end{bmatrix} \tag{a-3}$$

where H is the total enthalpy $H = h + \frac{1}{2}u^2$. The eigenvalues $\{\lambda_n\}$ are the root of the characteristic third-order polynomial resulting from

$$\det\left(\frac{\partial \mathbf{V}}{\partial \mathbf{U}}\frac{\partial \mathbf{E}}{\partial \mathbf{V}} - \lambda \mathbf{I}\right) = 0 \tag{a-4}$$

where $\mathbf{I}$ is the identity matrix, the matrix $\dfrac{\partial \mathbf{V}}{\partial \mathbf{U}}$ is the inverse of the matrix $\dfrac{\partial \mathbf{U}}{\partial \mathbf{V}}$. Since it is difficult to compute $\dfrac{\partial \mathbf{V}}{\partial \mathbf{U}}$ with the conservative variable set $\mathbf{U}$, we compute $\dfrac{\partial \mathbf{V}}{\partial \mathbf{U}}$ first, then take its inverse. Taking the various derivatives we find that

$$\frac{\partial \mathbf{U}}{\partial \mathbf{V}} = \begin{bmatrix} \rho_p & 0 & \rho_T \\ \rho_p u & \rho & \rho_T u \\ \rho_p H + \rho h_p - 1 & \rho u & \rho_T H + \rho h_T \end{bmatrix} \tag{a-5}$$

Taking the inverse of the above matrix results in

$$\frac{\partial \mathbf{V}}{\partial \mathbf{U}} = \begin{bmatrix} \dfrac{\rho_T H + \rho h_T - \rho_T u^2}{\rho\rho_p h_T - \rho\rho_T h_p + \rho_T} & \dfrac{\rho_T u}{\rho\rho_p h_T - \rho\rho_T h_p + \rho_T} & -\dfrac{\rho_T}{\rho\rho_p h_T - \rho\rho_T h_p + \rho_T} \\ -\dfrac{u}{\rho} & \dfrac{1}{\rho} & 0 \\ \dfrac{\rho_p u^2 - \rho_p H - \rho h_p + 1}{\rho\rho_p h_T - \rho\rho_T h_p + \rho_T} & \dfrac{-\rho_p u}{\rho\rho_p h_T - \rho\rho_T h_p + \rho_T} & \dfrac{\rho_p}{\rho\rho_p h_T - \rho\rho_T h_p + \rho_T} \end{bmatrix} \tag{a-6}$$

The matrix $\dfrac{\partial \mathbf{E}}{\partial \mathbf{V}}$ is obtained by taking the various derivatives,

$$\frac{\partial \mathbf{E}}{\partial \mathbf{V}} = \begin{bmatrix} \rho_p u & \rho & \rho_T u \\ \rho_p u^2 + 1 & 2\rho u & \rho_T u^2 \\ \rho_p H u + \rho h_p u & \rho H + \rho u^2 & \rho_T H u + \rho h_T u \end{bmatrix} \tag{a-7}$$

Thus $\dfrac{\partial \mathbf{V}}{\partial \mathbf{U}}\dfrac{\partial \mathbf{E}}{\partial \mathbf{V}}$ in Equation a-4 is obtained by multiplying $\dfrac{\partial \mathbf{V}}{\partial \mathbf{U}}$ by $\dfrac{\partial \mathbf{E}}{\partial \mathbf{V}}$:

$$\frac{\partial \mathbf{V}}{\partial \mathbf{U}}\frac{\partial \mathbf{E}}{\partial \mathbf{V}} = \begin{bmatrix} u & \dfrac{\rho^2 h_T}{\rho\rho_p h_T - \rho\rho_T h_p + \rho_T} & 0 \\ \dfrac{1}{\rho} & u & 0 \\ 0 & \dfrac{\rho - \rho^2 h_p}{\rho\rho_p h_T - \rho\rho_T h_p + \rho_T} & u \end{bmatrix} \tag{a-8}$$

The characteristic equation resulting from the evaluation of Equation a-4 is

$$(u-\lambda)\left[(u-\lambda)^2 - \frac{\rho h_T}{\rho\rho_p h_T - \rho\rho_T h_p + \rho_T}\right] = 0 \tag{a-9}$$

The roots of Equation a-9 are similar in form to the expected result if the ideal gas equation of state is used, in which a convective eigenvalue and two acoustic eigenvalues $(u, u \pm a)$ are returned.

$$\lambda_1 = u, \quad \lambda_{2,3} = u \pm \sqrt{\frac{\rho h_T}{\rho\rho_p h_T - \rho\rho_T h_p + \rho_T}} \tag{a-10}$$

From this analysis the speed of sound for a generalized equation of state is

$$a = \sqrt{\frac{\rho h_T}{\rho\rho_p h_T - \rho\rho_T h_p + \rho_T}} \tag{a-11}$$

which reverts to $a = \sqrt{\gamma \mathcal{R} T}$ when the ideal gas law is substituted as the equation of state.

B Eigenvalues of the Preconditioned System

The one-dimensional Euler system described in Appendix A can be preconditioned as:

$$\mathbf{P}\frac{\partial \mathbf{V}}{\partial t} + \frac{\partial \mathbf{E}}{\partial x} = 0 \tag{b-1}$$

where $\mathbf{P}$ is the preconditioning matrix obtained using the same method described in Section 2.1. It takes the form:

$$\mathbf{P} = \begin{bmatrix} \rho_p + \Theta & 0 & \rho_T \\ (\rho_p + \Theta)u & \rho & \rho_T u \\ (\rho_p + \Theta)H + \rho h_p - 1 & \rho u & \rho_T H + \rho h_T \end{bmatrix} \tag{b-2}$$

where

$$\Theta = \frac{1}{V_{ref}^2} - \frac{1}{a^2}. \tag{b-3}$$

V_{ref}^2 is the reference velocity as defined in Equation 2.7, and a is the real fluid sound speed as defined in Equation a-11.

The eigenvalues of the preconditioned system, i.e., $\mathbf{P}^{-1}\frac{\partial \mathbf{E}}{\partial \mathbf{V}}$, are obtained using the same procedure described in Appendix A. These eigenvalues are

$$u, \quad \text{and} \quad u' \pm a' = \frac{1 + M_{ref}^2}{2}\left[u \pm a\frac{\sqrt{\left(1 - M_{ref}^2\right)^2 M^2 + 4M_{ref}^2}}{1 + M_{ref}^2}\right], \tag{b-4}$$

where

$$M_{ref} = \frac{V_{ref}}{a}, \quad M = \frac{u}{a} \tag{b-5}$$

are the reference Mach number and the Mach number respectively.

Several remarks can be made concerning the eigenvalues of the preconditioned system. Firstly, we have a bound for the coefficient,

$$\frac{1}{2} < \frac{1 + M_{ref}^2}{2} \leqslant 1, \tag{b-6}$$

Secondly, the speed of sound is now re-scaled by a factor, $f(M, M_{ref})$. Thus, a new speed of sound can be defined as:

$$\tilde{a} = f(M, M_{ref})a, \tag{b-7}$$

$$f(M, M_{ref}) = \frac{\sqrt{\left(1 - M_{ref}^2\right)^2 M^2 + 4M_{ref}^2}}{1 + M_{ref}^2}. \tag{b-8}$$

The scaling factor is bounded as,

$$1 \geqslant f \geqslant \begin{cases} |M|, & \text{if } 1 \gg M^2 \gg M_{ref}^2, \\ 2M_{ref}, & \text{if } 1 \gg M_{ref}^2 \gg M^2. \end{cases} \tag{b-9}$$

C Interface Flux Jacobian Matrices

The matrices A-G used in Section 2.4 are functions of the inviscid and viscous flux Jacobians. Appendix C introduces an implicit formulation to construct these matrices [9].

Implicit techniques for integrating the unsteady Navier-Stokes equations can generally be viewed as approximations to Newton's method for solving the steady Navier-Stokes equations. A local time linearization of the nonlinear system is usually required. Besides, a matrix inversion procedure for solving the linear system at each time level is required too.

A nearly exact first-order linearization of the LDFSS interface flux $\mathbf{E}_{i+\frac{1}{2}}$ (in ξ direction) in terms of the primitive variable set $\mathbf{V}$ as defined in Equation 2.2 can be constructed by defining

$$\frac{\partial \mathbf{E}_{i+\frac{1}{2}}}{\partial \mathbf{V}_{i+\frac{1}{2}}} \Delta V_{i+\frac{1}{2}} = A^+_{i+\frac{1}{2}} \Delta V_i + A^-_{i+\frac{1}{2}} \Delta V_{i+1}, \tag{c-1}$$

where

$$A^+_{i+\frac{1}{2}} = \frac{\partial \mathbf{E}_{i+\frac{1}{2}}}{\partial \mathbf{V}_i}, \quad A^-_{i+\frac{1}{2}} = \frac{\partial \mathbf{E}_{i+\frac{1}{2}}}{\partial \mathbf{V}_{i+1}}. \tag{c-2}$$

and $\mathbf{E}_{i+\frac{1}{2}}$ is the interface flux as defined in Equation 2.23, and is rewritten here:

$$\begin{aligned} \mathbf{E}_{i+\frac{1}{2}} &= \mathbf{E}^c_{i+\frac{1}{2}} + \mathbf{E}^p_{i+\frac{1}{2}}, \\ \mathbf{E}^c_{i+\frac{1}{2}} &= \frac{|\nabla \xi|}{J} \left(U^+ \Phi_i + U^- \Phi_{i+1} \right), \\ \mathbf{E}^p_{i+\frac{1}{2}} &= \frac{|\nabla \xi|}{J} P_{\frac{1}{2}} \Psi_i. \end{aligned} \tag{c-3}$$

The quantities used in the above equations are defined in Section 2.3.1. The direct calculations of the above expressions that result from the differentiation (holding $\alpha^{\pm}$ and β locally constant) are rather complicated and expensive to compute. A simpler, approximate linearization with good stability properties can be derived by contracting the exact expressions for the 'positive' and 'negative' flux Jacobians $A^{+}_{i+\frac{1}{2}}$ and $A^{-}_{i+\frac{1}{2}}$ to the single grid nodes i and $i+1$, respectively. This leads to the following implicit representation:

$$\frac{\partial \mathbf{E}_{i+\frac{1}{2}}}{\partial \mathbf{V}_{i+\frac{1}{2}}} \Delta V_{i+\frac{1}{2}} = A^{+}_{i} \Delta V_{i} + A^{-}_{i+1} \Delta V_{i+1}, \tag{c-4}$$

where $A^{\pm}_{i}$ may be expressed as

$$A^{\pm}_{i} = \frac{1}{2} \left[\frac{\partial \mathbf{E}_{i}}{\partial \mathbf{V}_{i}} \pm \left(\left. \frac{\partial \mathbf{E}_{i+\frac{1}{2}}}{\partial \mathbf{V}_{i}} \right|_{i} - \left. \frac{\partial \mathbf{E}_{i+\frac{1}{2}}}{\partial \mathbf{V}_{i+1}} \right|_{i} \right) \right]. \tag{c-5}$$

The last two terms in Equation c-5 are both contracted to grid node i to get a simpler expression for Jacobian matrix. $\mathbf{E}_{i}$ is the actual flux as defined in Equation 2.20, and rewritten here,

$$\mathbf{E}_{i} = \mathbf{E}^{c}_{i} + \mathbf{E}^{p}_{i} = \frac{|\nabla \xi|}{J} \left(\overline{\mathcal{U}} \Phi_{i} + p_{i} \Psi_{i} \right). \tag{c-6}$$

Thus, the differentiation of $\mathbf{E}_{i}$ is obtained as

$$\frac{\partial \mathbf{E}_{i}}{\partial \mathbf{V}_{i}} = \frac{|\nabla \xi|}{J} \left[\overline{\mathcal{U}} \left(\frac{\partial \Phi}{\partial \mathbf{V}} \right)_{i} + \Phi_{i} \Psi^{T}_{i} + \Psi_{i} \vec{v}^{T} \right], \tag{c-7}$$

where

$$\vec{v} = \frac{\partial p}{\partial \mathbf{V}} = \begin{bmatrix} \partial p / \partial Y_{g,1} \\ \vdots \\ \partial p / \partial Y_{g,N_g - 1} \\ \partial p / \partial Y_{g} \\ \partial p / \partial p \\ \partial p / \partial u \\ \partial p / \partial v \\ \partial p / \partial w \\ \partial p / \partial T \\ \partial p / \partial Y_{l,1} \\ \vdots \\ \partial p / \partial Y_{l,N_l - 1} \end{bmatrix} = \begin{bmatrix} 0 \\ \vdots \\ 0 \\ 0 \\ 1 \\ 0 \\ 0 \\ 0 \\ 0 \\ 0 \\ \vdots \\ 0 \end{bmatrix} \tag{c-8}$$

After some steps of derivation, the linearization of flux Jacobians can be obtained by index contraction as follows:

$$\begin{aligned}\left.\frac{\partial \mathbf{E}_{i+\frac{1}{2}}}{\partial \mathbf{V}_i}\right|_i - \left.\frac{\partial \mathbf{E}_{i+\frac{1}{2}}}{\partial \mathbf{V}_{i+1}}\right|_i &= \frac{|\nabla\xi|}{J}\left[\tilde{a}_{\frac{1}{2}}\left|M_i\right|\left(\frac{\partial \Phi}{\partial \mathbf{V}}\right)_i + \Phi_i r^T + \Psi_i s^T\right] \\ &= \frac{|\nabla\xi|}{J}\left[\left|\overline{\mathcal{U}}\right|\left(\frac{\partial \Phi}{\partial \mathbf{V}}\right)_i + \Phi_i r^T + \Psi_i s^T\right], \end{aligned} \tag{c-9}$$

where

$$r = \begin{bmatrix} 0 \\ \vdots \\ 0 \\ 0 \\ 2\tilde{a}_{\frac{1}{2}} M_{\frac{1}{2}}/(\rho_i V_{ref}^2) \\ \xi_x\left[(1+\beta_i)\,\mathrm{sign}\left(M_i\right) - \beta_i M_i\right] \\ \xi_y\left[(1+\beta_i)\,\mathrm{sign}\left(M_i\right) - \beta_i M_i\right] \\ \xi_z\left[(1+\beta_i)\,\mathrm{sign}\left(M_i\right) - \beta_i M_i\right] \\ 0 \\ 0 \\ \vdots \\ 0 \end{bmatrix}, \quad s = \begin{bmatrix} 0 \\ \vdots \\ 0 \\ 0 \\ (1+\beta_i)\,\mathrm{sign}\left(M_i\right) - \beta_i M_i \\ -\xi_x \beta_i \rho_{\frac{1}{2}} V_{ref}^2 g'\left(M_i\right)/\tilde{a}_{\frac{1}{2}} \\ -\xi_y \beta_i \rho_{\frac{1}{2}} V_{ref}^2 g'\left(M_i\right)/\tilde{a}_{\frac{1}{2}} \\ -\xi_z \beta_i \rho_{\frac{1}{2}} V_{ref}^2 g'\left(M_i\right)/\tilde{a}_{\frac{1}{2}} \\ 0 \\ 0 \\ \vdots \\ 0 \end{bmatrix}. \tag{c-10}$$

Finally, the flux Jacobians $A_i^{\pm}$ may be expressed as

$$A_i^{\pm} = \frac{|\nabla\xi|}{2J}\left[\left(\overline{\mathcal{U}} \pm \left|\overline{\mathcal{U}}\right|\right)\left(\frac{\partial \Phi}{\partial \mathbf{V}}\right)_i + \Phi_i\left(\Psi_i^T \pm r^T\right) + \Psi_i\left(\vec{v}^T \pm s^T\right)\right], \tag{c-11}$$

where $\dfrac{\partial \Phi}{\partial \mathbf{V}}$ can be expressed as

$$\frac{\partial \Phi}{\partial \mathbf{V}} =$$

$$\begin{bmatrix}
\rho Y_g + \rho_{Y_{g,1}} Y_{g,1} Y_g & \cdots & \rho_{Y_{g,N_g-1}} Y_{g,1} Y_g & \rho Y_{g_1} + \rho_{Y_g} Y_{g,1} Y_g & \rho_p Y_{g,1} Y_g \\
\vdots & \ddots & \vdots & \vdots & \vdots \\
\rho_{Y_{g,1}} Y_{g,N_g-1} Y_g & \cdots & \rho Y_g + \rho_{Y_{g,N_g-1}} Y_{g,N_g-1} Y_g & \rho Y_{g,N_g-1} + \rho_{Y_g} Y_{g,N_g-1} Y_g & \rho_p Y_{g,N_g-1} Y_g \\
\rho_{Y_{g,1}} Y_g & \cdots & \rho_{Y_{g,N_g-1}} Y_g & \rho + \rho_{Y_g} Y_g & \rho_p Y_g \\
\rho_{Y_{g,1}} & \cdots & \rho_{Y_{g,N_g-1}} & \rho_{Y_g} & \rho_p \\
\rho_{Y_{g,1}} u & \cdots & \rho_{Y_{g,N_g-1}} u & \rho_{Y_g} u & \rho_p u \\
\rho_{Y_{g,1}} v & \cdots & \rho_{Y_{g,N_g-1}} v & \rho_{Y_g} v & \rho_p v \\
\rho_{Y_{g,1}} w & \cdots & \rho_{Y_{g,N_g-1}} w & \rho_{Y_g} w & \rho_p w \\
\rho_{Y_{g,1}} H + \rho h_{Y_{g,1}} & \cdots & \rho_{Y_{g,N_g-1}} H + \rho h_{Y_{g,N_g-1}} & \rho_{Y_g} H + \rho h_{Y_g} & \rho_p H + \rho h_p \\
\rho_{Y_{g,1}} Y_{l,1} Y_l & \cdots & \rho_{Y_{g,N_g-1}} Y_{l,1} Y_l & -\rho Y_{l_1} + \rho_{Y_g} Y_{l,1} Y_l & \rho_p Y_{l,1} Y_l \\
\vdots & \vdots & \vdots & \vdots & \vdots \\
\rho_{Y_{g,1}} Y_{l,N_l-1} Y_l & \cdots & \rho_{Y_{g,N_g-1}} Y_{l,N_l-1} Y_l & -\rho Y_{l,N_l-1} + \rho_{Y_g} Y_{l,N_l-1} Y_l & \rho_p Y_{l,N_l-1} Y_l
\end{bmatrix}$$

$$\begin{bmatrix}
0 & 0 & 0 & \rho_T Y_{g,1} Y_g & \rho_{Y_{l,1}} Y_{g,1} Y_g & \cdots & \rho_{Y_{l,N_l-1}} Y_{g,1} Y_g \\
\vdots & \vdots & \vdots & \vdots & \vdots & \vdots & \vdots \\
0 & 0 & 0 & \rho_T Y_{g,N_g-1} Y_g & \rho_{Y_{l,1}} Y_{g,N_g-1} Y_g & \cdots & \rho_{Y_{l,N_l-1}} Y_{g,N_g-1} Y_g \\
0 & 0 & 0 & \rho_T Y_g & \rho_{Y_{l,1}} Y_g & \cdots & \rho_{Y_{l,N_l-1}} Y_g \\
0 & 0 & 0 & \rho_T & \rho_{Y_{l,1}} & \cdots & \rho_{Y_{l,N_l-1}} \\
\rho & 0 & 0 & \rho_T u & \rho_{Y_{l,1}} u & \cdots & \rho_{Y_{l,N_l-1}} u \\
0 & \rho & 0 & \rho_T v & \rho_{Y_{l,1}} v & \cdots & \rho_{Y_{l,N_l-1}} v \\
0 & 0 & \rho & \rho_T w & \rho_{Y_{l,1}} w & \cdots & \rho_{Y_{l,N_l-1}} w \\
\rho u & \rho v & \rho w & \rho_T H + \rho h_T & \rho_{Y_{l,1}} H + \rho h_{Y_{l,1}} & \cdots & \rho_{Y_{l,N_l-1}} H + \rho h_{Y_{l,N_l-1}} \\
0 & 0 & 0 & \rho_T Y_{l,1} Y_l & \rho Y_l + \rho_{Y_{l,1}} Y_{l,1} Y_l & \cdots & \rho_{Y_{l,N_l-1}} Y_{l,1} Y_l \\
\vdots & \vdots & \vdots & \vdots & \vdots & \ddots & \vdots \\
0 & 0 & 0 & \rho_T Y_{l,N_l-1} Y_l & \rho_{Y_{l,1}} Y_{l,N_l-1} Y_l & \cdots & \rho Y_l + \rho_{Y_{l,N_l-1}} Y_{l,N_l-1} Y_l
\end{bmatrix} \quad \text{(c-12)}$$